The Astrophysical Journal, 805:3 (19pp), 2015 May 20 doi:10.1088/0004-637X/805/1/3

ARE THE EFFECTS OF STRUCTURE FORMATION SEEN IN THE CENTRAL METALLICITY OF GALAXY CLUSTERS?

Tamer Y. Elkholy[1,2], Mark W. Bautz[2], and Claude R. Canizares[1,2]
[1] Department of Physics, Massachusetts Institute of Technology, 77 Massachusetts Avenue, Cambridge, MA 02139, USA; tykholy@gmail.com
[2] MIT Kavli Institute for Astrophysics and Space Research, 77 Massachusetts Avenue, Cambridge, MA 02139, USA

Received 2014 July 14; accepted 2015 March 9; published 2015 May 13

ABSTRACT

A sample of 46 nearby clusters observed with *Chandra* is analyzed to produce radial density, temperature, entropy, and metallicity profiles, as well as other morphological measurements. The entropy profiles are computed to larger radii than in previous *Chandra* cluster sample analyses. We find that the iron mass fraction measured in the inner $0.15R_{500}$ shows a larger dispersion across the sample of low-mass clusters than it does for the sample of high-mass clusters. We interpret this finding as the result of the mixing of more halos in large clusters than in small clusters, leading to an averaging of the metallicity in the large clusters, and thus less dispersion of metallicity. This interpretation lends support to the idea that the low-entropy, metal-rich gas of merging halos reaches the clusters' centers, which explains observations of core-collapse supernova product metallicity peaks, and which is seen in hydrodynamical simulations. The gas in these merging halos would have to reach cluster centers without mixing in the outer regions. On the other hand, the metallicity dispersion does not change with mass in the outer regions of the clusters, suggesting that most of the outer metals originate from a source with a more uniform metallicity level, such as during pre-enrichment. We also measure a correlation between the metal content in low-mass clusters and the morphological disturbance of their intracluster medium, as measured by centroid shift. This suggests an alternative interpretation, whereby transitional metallicity boosts in the center of low-mass clusters account for the larger dispersion of their metallicities.

Key words: galaxies: clusters: general – galaxies: clusters: intracluster medium – X-rays: galaxies: clusters

Supporting material: extended figures, machine-readable tables

1. INTRODUCTION

In today's universe, galaxy clusters are the largest bound structures, ranging in mass from about 10^{13} to $10^{15}\ M_\odot$. Their formation is understood within the paradigm of hierarchical structure formation, where large structures form through the merger of smaller structures. Because of their large masses, the intracluster medium (ICM) in galaxy clusters is heated and compressed, such that bremsstrahlung emission becomes an efficient radiation process. This X-ray emission from the ICM contains within it ample information about the chemistry and the dynamical state of the ICM, and by extension the cluster as a whole. In particular we focus in this study on two quantities, metallicity and entropy, because they encode the integrated effect of various physical processes occurring in clusters.

Most metals have been produced in stars, predominantly through thermonuclear burning, or in processes resulting from the extreme conditions in supernovae (SNe). Therefore, studying metallicity in galaxy clusters probes processes that produce metals, such as star formation and supernova (SN) rates, as well as processes that mix and distribute metals such as mergers and central active galactic nucleus (AGN) activity.

Renzini et al. (1993) were the first to point out that one cannot account for all of the observed metals in the ICM by assuming that the current SN type Ia rate per unit luminosity was the same in the past. This problem was studied with better SN data and more complex chemical evolution and ICM enrichment models by Portinari et al. (2004) and Loewenstein (2006), who both showed the need for more metal production in clusters, compared to what is observed in the field. Both studies above, in addition to Nagashima et al. (2005), suggest that a different stellar initial mass function (IMF) must operate in field galaxies than in clusters. For example, a top-heavy IMF might be necessary in galaxy clusters.

Hydrodynamical models predicting the metallicity of the ICM have been reviewed by Borgani et al. (2008). The results of these studies vary in terms of the effect of different IMFs on the level of enrichment, as some are able to match or even exceed the observed metallicity in clusters, while others cannot match it, depending on the many details and parameters of the models.

Two classes of SNe are responsible for producing the metals in clusters. Core-collapse SNe (SNCC) result from massive stars, whose lives are short compared to the time since the peak of star formation, at a redshift of $z \sim 2-3$. Type Ia SNe (SNIa) result from low-mass stars and thus can be delayed by billions of years from the time of star formation. If the above picture of a prompt metal injection from SNCC followed by a more gradual injection from SNIa holds, then we should expect this to affect the metallicity radial profiles. Each class of SNe produces a different set of elements (e.g., Werner et al. 2008). Both SN classes produce iron, but, for example, SNCC are the main contributors of oxygen, neon, and magnesium. Becaue the rate of SNCC at any epoch is roughly proportional to the then-current rate of star formation, and because clusters form relatively late, we expect SNCC products to have enriched the proto-ICM before cluster collapse. The SNCC products are therefore expected to be homogeneously spread through the ICM. Conversely, SNIa products are expected to be nearer the center of the cluster, as the brightest cluster galaxy accumulates more and more stars with time. However, using very deep *Chandra* observations, Sanders & Fabian (2006), Simionescu et al. (2008a, 2010), and Million et al. (2011) measure a large amount of SNCC products in the core of nearby galaxy clusters, presenting a challenge to the above picture.

Because entropy remains unchanged under adiabatic processes, it measures any heat input or output to the gas. In the case of the ICM, the main process that changes its entropy is gravitational shock heating. Other processes affecting the ICM entropy include radiative cooling, heating by AGN and SNe, as well as processes such as turbulent dissipation and conduction. The reader is referred to McNamara & Nulsen (2007) for a detailed review of the above processes.

Gravity is expected to be the dominant force in cluster formation, and thus most of the entropy generation is expected to result from shock heating of infalling gas as a cluster forms. This process converts gravitational potential energy into heat. Because $S \propto T/n^{2/3}$, we expect the characteristic entropy scale of a cluster to scale proportionally to its virial temperature, or as $M^{2/3}$, where M is the cluster mass. Hydrodynamical simulations (e.g., Voit et al. 2005; Nagai et al. 2007) produce a normalization of the entropy expected from gravity, as well as a radial profile, which is proportional to a power law of radius $r^{1.1-1.2}$. Observationally, Ponman et al. (1999) were among the first to measure the departure of the entropy from the expected self-similar scaling with cluster mass. The same result was later found in Lloyd-Davies et al. (2000), Ponman et al. (2003), and Pratt et al. (2010).

Some studies have focused on cases where the effects of both heating and metal enrichment can be detected. High-resolution observations of the centers of clusters find regions of enhanced metallicity expected to have been ejected from the central regions of clusters by the central engine (e.g., Simionescu et al. 2008a, 2009; Kirkpatrick et al. 2009; O'Sullivan et al. 2011). For example, Kirkpatrick et al. (2011) showed that the direction of elongation of an enhanced-metallicity region is correlated with the direction of cavities and radio emission axes originating from the center. On larger scales, however, simulations by Borgani et al. (2005) and Short et al. (2013) suggest that winds from SNe have little effect on the overall entropy of clusters. There is, however, a shortage of attempts to test these results observationally.

The aim of this work is therefore to apply a systematic, spatially resolved study of metallicity and entropy to a large sample of galaxy clusters, to look for any possible relation between the metallicity and the entropy of the ICM. We also aim to produce a data set of entropy profiles (in the form of temperature and metallicity profiles) for the community to employ in various galaxy cluster studies and make it available electronically.

Throughout this work, a ΛCDM cosmological model is assumed, where the Hubble constant is $H_0 = 72\ \mathrm{km\,s^{-1}\,Mpc^{-1}}$, the matter density parameter is $\Omega_m = 0.26$, the dark energy density is $\Omega_\Lambda = 0.74$, and the universal baryon fraction is $f_b = \Omega_b/\Omega_m = 0.169$, where Ω_b is the baryon density.

2. DATA SAMPLE AND ANALYSIS

2.1. Data Sample

Our sample consists of bright clusters—present in both the HIFLUGCS and ACCEPT samples—that were observed with *Chandra*'s ACIS instrument out to at least $0.2R_{500}$, where R_{500} is the radius enclosing an average density that is 500 times the critical density of the universe at the redshift of the observed cluster. More precisely, we start with the extended HIFLUGCS sample of galaxy clusters, which is a flux-limited sample of clusters with X-ray flux $f_X\,[0.1 - 2.4\ \mathrm{keV}] \geqslant 2 \times 10^{-11}\ \mathrm{erg\,s^{-1}\,cm^{-2}}$ (Reiprich & Böhringer 2002). We search for the HIFLUGCS clusters that have *Chandra* coverage[3] out to at least $0.2R_{500}$. Once the sample is identified, we search the ACCEPT data for the aforementioned HIFLUGCS subsample, where entropy is measured in at least three radial bins beyond $0.2R_{500}$. The ACCEPT study (Cavagnolo et al. 2009) measured the entropy profiles of all galaxy clusters observed by *Chandra*, up to 2008 August, and has made the data available online.[4] Forty-eight galaxy clusters satisfy the above selection criteria.

For all spectral analysis, we discard all observations taken before 2000 January 29 because the *Chandra* focal plane temperature for that period was −110° C or higher, which increases the level of background. *Chandra*'s calibration is in general better for later dates. Only one cluster, Abell 401, is excluded from our analysis because it was only observed prior to 2000 January 29. We also exclude Abell 2255 because its available observation was too short to yield enough photons. The complete analysis will thus be presented for a sample of 46 clusters.

We show in Table 1 the observational details of our sample and the *Chandra* observations used in this work. For each cluster, we show the label that will be used to designate it hereafter in figures and tables. We show the cluster's celestial coordinates and its redshift. We list the *Chandra* observation IDs (OBSID) we use in this work. Some OBSIDs are shown in parentheses. These are the observations that were used in the imaging analysis and excluded from the spectral analysis, as described above. Finally, we show the total exposure time used in the spectral analysis of each cluster.

2.2. Data Preparation

We use the Chandra Interactive Analysis of Observations software, more commonly known as CIAO,[5] for analysis in this work. More precisely, we use CIAO version 4.2. Data are reprocessed following the guidelines in the CIAO analysis thread "Reprocessing Data to Create New Level = 2 Event File," using the tool `acis_process_events`. This reprocessing includes filtering to keep only event grades 0, 2, 3, 4, and 6. In addition, the VFAINT background cleaning method is applied to observations in VFAINT mode, using the `check_vf_pha = yes` option to `acis_process_events`.

The center of the clusters is defined to be the centroid of event x and y coordinates, calculated using the following iterative scheme. First, we select the observation with the longest exposure time in the cases where we have multiple observations of one cluster. For ACIS-I pointing, we calculate the centroid using all four ACIS-I chips, and for ACIS-S pointings, we only use the chip with the most counts. We only include events with energies between 0.3 and 7 keV. For the first centroid computation iteration, Iteration 1, we calculate the medians and the standard deviations of the x and y coordinates of the events from the entirety of the selected chip(s) of the longest-exposure observation. For Iteration 2, we restrict the median and standard deviation calculation to events within an

---

[3] For the purpose of selecting clusters, we use the values of R_{500} measured in Reiprich & Böhringer (2002).

[4] http://www.pa.msu.edu/astro/MC2/accept/

[5] http://cxc.harvard.edu/ciao/

Table 1
Chandra Observations

Cluster[a]	Label[b]	R.A.[c]	Decl.[d]	z[e]	OBSIDs[f]	T (ks)[g]
Abell 119	a119	00:56:15.392	−01:15:17.78	0.044	4180, 7918	57
Abell 1413	a1413	11:55:17.986	+23:24:17.82	0.1427	1661, 5002, 5003	121
Abell 1644	a1644	12:57:11.772	−17:24:33.68	0.0474	2206, 7922	70
Abell 1651	a1651	12:59:22.188	−04:11:45.80	0.086	4185	10
Abell 1689	a1689	13:11:29.495	−01:20:29.02	0.184	5004, 540, 6930, 7289	181
Abell 1736	a1736	13:26:54.235	−27:09:48.65	0.0461	10428, 10429, 10430, 10431, 4186	35
Abell 1795	a1795	13:48:52.668	+26:35:30.73	0.0616	10898, 10899, 10900, 10901, 12026, 12028, 12029, 13106, 13107, 13108, 13109, 13110, 13111, 13112, 13113, 13412, 13413, 13414, 13415, 13416, 13417, 5286, 5287, 5288, 6159, 6160, 6161, 6162, 6163, (494)	437
Abell 1914	a1914	14:26:01.072	+37:49:32.97	0.1712	3593, (542)	27
Abell 2029	a2029	15:10:56.091	+05:44:40.94	0.0767	10437, 4977, 6101, 891	112
Abell 2063	a2063	15:23:05.323	+08:36:28.49	0.0354	5795, 6263	27
Abell 2065	a2065	15:22:29.060	+27:42:34.33	0.0721	3182	22
Abell 2142	a2142	15:58:20.103	+27:13:58.76	0.0899	5005, (1196, 1228)	68
Abell 2147	a2147	16:02:15.608	+15:57:53.77	0.0351	3211	18
Abell 2163	a2163	16:15:46.519	−06:08:50.57	0.201	1653, 2455, 545	89
Abell 2204	a2204	16:32:46.922	+05:34:31.40	0.1523	499, 6104, 7940	97
Abell 2244	a2244	17:02:42.517	+34:03:37.46	0.097	4179	57
Abell 2256	a2256	17:03:59.388	+78:38:44.57	0.0601	2419, (1386, 965)	35
Abell 2319	a2319	19:21:09.997	+43:57:18.82	0.0564	3231	14
Abell 2657	a2657	23:44:56.531	+09:11:28.75	0.0404	4941	16
Abell 2734	a2734	00:11:21.616	−28:51:17.98	0.062	5797	20
Abell 3112	a3112	03:17:57.627	−44:14:20.34	0.075	2216, 2516, 6972, 7323, 7324	108
Abell 3158	a3158	03:42:52.591	−53:37:50.03	0.059	3201, 3712	56
Abell 3376	a3376	06:01:57.312	−39:58:25.80	0.0455	3202, 3450	64
Abell 3391	a3391	06:26:20.780	−53:41:32.98	0.0531	4943	18
Abell 3571	a3571	13:47:28.580	−32:51:14.35	0.0397	4203	34
Abell 3667	a3667	20:12:36.316	−56:50:40.74	0.056	5751, 5752, 6292, 6295, 6296, 889, (513)	430
Abell 3822	a3822	21:54:06.292	−57:51:41.06	0.076	8269	8
Abell 3827	a3827	22:01:53.279	−59:56:45.99	0.098	7920	46
Abell 3921	a3921	22:49:57.845	−64:25:44.13	0.0936	4973	29
Abell 399	a399	02:57:51.557	+13:02:32.43	0.0715	3230	49
Abell 400	a400	02:57:41.119	+06:01:20.03	0.024	4181	21
Abell 4038	a4038	23:47:43.200	−28:08:38.30	0.0283	4188, 4992	40
Abell 4059	a4059	23:57:00.933	−34:45:34.44	0.046	5785, 897	110
Abell 478	a478	04:13:25.199	+10:27:53.90	0.09	1669, 6102	52
Abell 539	a539	05:16:36.680	+06:26:34.63	0.0288	5808, 7209	43
Abell 644	a644	08:17:25.392	−07:30:48.38	0.0704	10420, 10421, 10422, 10423, 2211	49
Abell 754	a754	09:09:21.084	−09:41:05.78	0.0528	10743, 6793, 6794, 6796, 6797, 6799, (577)	187
Abell S 405	as405	03:51:29.787	−82:13:21.26	0.0613	8272	8
Hydra A	hyda	09:18:05.876	−12:05:43.17	0.0538	4969, 4970, (575, 576)	239
Zw III 54	iiizw54	03:41:17.508	+15:23:54.82	0.0311	4182	23
MKW 3S	mkw3s	15:21:51.708	+07:42:24.65	0.045	900	57
MKW 8	mkw8	14:40:39.353	+03:28:03.08	0.027	4942	23
PKS 0745–191	pks0745–191	07:47:31.265	−19:17:41.62	0.1028	2427, 508, 6103	56
UGC 3957	ugc3957	07:40:58.133	+55:25:38.25	0.034	8265	8
ZwCl 1215 + 0400	z1215	12:17:41.934	+03:39:39.74	0.075	4184	12
ZwCl 1742 + 3306	z1742	17:44:14.447	+32:59:29.02	0.0757	11708, 8267	53

[a] Cluster name.

[b] Label used to denote cluster.

[c] Cluster right ascension.

[d] Cluster declination.

[e] Cluster redshift.

[f] The *Chandra* OBSIDs used in this work. OBSIDs in parentheses were used in imaging analysis and excluded from spectral analysis.

[g] The total exposure time for spectral analysis in kiloseconds.

(This table is available in machine-readable form.)

ellipse with semimajor axes equal to *twice* the x and y standard deviations calculated in Iteration 1, i.e., $2 \times (\sigma_{x1}, \sigma_{y1})$. For Iteration 3, the ellipse is shrunk to have semimajor axes equal to $1 \times (\sigma_{x2}, \sigma_{y2})$. Similarly, Iteration 4's filter ellipse has semimajor axes $0.75 \times (\sigma_{x3}, \sigma_{y3})$. For the final iteration, Iteration 5, we employ events from all observations in the centroid computation, instead of using the longest-exposure observation alone. The Iteration 5 filter ellipse has semimajor axes equal to $1 \times (\sigma_{x4}, \sigma_{y4})$.

Events from point sources are then identified and discarded. We use CIAO's `wavdetect` tool, applied to an image of the merged event files from all observations. The input image to `wavdetect` includes only events with energies in the range 0.3–7 keV and is binned in (2×2)-pixel bins. The detected point-source regions are inspected by eye to ensure that each region is large enough to include all events from its corresponding detected point source and to add sources that were not detected by `wavdetect`. The latter tend to be point sources away from the telescope's optical axis, where the point-spread function is much larger than it is in the center. We also exclude any region of bright extended emission, which does not belong to the central cluster emission, such as that from infalling subclusters (e.g., the subcluster to the north of Abell 2163). We expect that many clusters will contain emission from faint infalling subclusters, which cannot be resolved due to their low surface brightness (SB). Therefore we do not attempt to discard all emission from identified subclusters, and we only remove the bright peaks of such emission when present.

Periods of high count rates resulting from flares are removed using the `lc_clean()` tool in *Sherpa*, which is CIAO's tool for spectral analysis. We compute a light curve of all data counts, excluding the point sources detected above and the central 300" to exclude the bulk of the cluster emission. Short flares are excluded when they are identified by `lc_clean()`, and longer flares are excluded manually by selecting events in the time range that is sufficiently removed from the start or the end of the flare. Some observations in which one or many flares last for most of the exposure time are entirely excluded.

For each observation, we create a background data set from the blank-sky files, available as part of the *Chandra* calibration files. We choose the blank-sky file for each ACIS chip based on the cluster data set's observation date, its aim point, and whether a CTI correction was applied to it. As mentioned above, we exclude all data taken prior to 2000 January 29. No blank-sky data sets are available in Period C in VFAINT mode. We therefore assign to these data sets the blank-sky files from Period D in VFAINT mode. In addition, we exclude some ACIS-S data taken during Period C because their corresponding blank-sky files are not available.[6]

2.3. Data Analysis

As is the custom in clusters astrophysics, we define entropy as $S = kT/n_e^{2/3}$, where k is Boltzmann's constant, T the ICM temperature, and n_e its electron density. As defined above, S is related to the thermodynamical entropy per particle, s, through $s = (3k/2)\ln S + s_0$, where s_0 only depends on fundamental constants. We assume spherical symmetry and compute the entropy radial profiles from the density and temperature profiles, as described below.

2.3.1. Density Profile, $n_e(r)$

Computation of the electron density profile of the ICM is done in two steps. First, we use SB measurements to constrain the shape of the density radial profile. Then, we use spectral measurements to set the overall normalization of $n_e(r)$. To fit for the density profile shape, we extract an SB profile based on photon counts in the energy range 0.7–2 keV. Radial bins are defined such that boundary radii are spaced logarithmically, with a constant ratio of 1.25 between neighboring radii, except when this spacing results in fewer than 100 counts in the bin, in which case it is extended to the next radius. The innermost radius is defined as the projection of 1.2 arcseconds in the plane of the cluster, in order to include the largest number of counts, while avoiding any potential point source coinciding with the centroid of the ICM X-ray emission. From the source counts in each radial bin, we subtract the background contribution computed from the blank-sky data sets and scale by detector area and exposure time to match each observation and radial bin. The net number of counts is then normalized by the exposure map, to correct for the position dependence of *Chandra*'s effective area. Finally, we obtain a count SB by dividing by the solid angle of the extraction region.

The emissivity of an X-ray plasma at cluster temperatures is primarily in the form of bremsstrahlung and line emission. The contribution of each of those processes is proportional to n_e^2, but depends differently on the plasma temperature. However, when emissivity is integrated over the 0.7–2 keV energy range, the different temperature dependencies contrive to cancel each other, and the resulting emission in this energy band has a negligible temperature dependence. In addition, we assume the ICM to be optically thin. Therefore, the SB at any given point on the sky is simply the integral of all emission along the line of sight (LOS) to that point. We perform a maximum-likelihood fit to find the density profile that best fits the counts SB profile, up to a normalization. We use an analytical form for $n_e(r)$ that is flexible enough to allow us to phenomenologically fit the SB in all radial bins. Namely, we choose a simplified version of Vikhlinin's extended beta model (Vikhlinin et al. 2006):

$$\frac{n_e^2(r)}{n_0^2} = \frac{\left(\frac{r}{r_c}\right)^{-\alpha}}{\left(1 + \frac{r^2}{r_c^2}\right)^{3\beta-\alpha/2}} \frac{1}{\left[1 + \left(\frac{r}{r_s}\right)^3\right]^{\epsilon/3}}, \tag{1}$$

where n_0, r_c, β, α, r_s, and ϵ are fit parameters. In each iteration of the fitting process, and for a given radial bin bound by radii r_i and r_{i+1}, we integrate $n_e^2(r)$ over the volume of the cylindrical shell defined by the above two radii and extending along the LOS from −3 to +3 Mpc. The set of integrals from all radial bins is then compared to the corresponding SB values to determine the shape parameters in the right-hand side of Equation (1).

This procedure provides the shape but not the normalization, n_0, of the density profiles. Computing n_0 requires knowledge of the emission integral measure, $EI = \int n_e n_p dV$, where n_p is the proton number density. This integral quantity, EI, is simply proportional to the normalization of the APEC spectral model,

---

[6] The definition of the background periods used here is available in Maxim Markevitch's note at http://cxc.harvard.edu/contrib/maxim/acisbg/COOKBOOK

which we use to model ICM emission. The APEC model (Smith et al. 2001) is fit to the spectra of multiple radial bins around the center of emission. The normalization of the spectral model of the ith radial bin, K_i, is related to EI_i through

$$K_i = \frac{0.82\ 10^{-14}}{4\pi D_A^2 (1+z)^2}\ n_0^2 V_i, \tag{2}$$

where z is the cluster redshift and D_A its angular diameter distance. We define V_i as the spatial integral of $(n/n_0)^2$ over the cylinder defined by the ith radial bin and bounded along the LOS direction by $\ell = \pm 20$ Mpc. We assumed above that $n_e = 0.82 n_p$, which is suitable for typical ICM conditions. The best-fit n_0 is determined by minimizing

$$\chi^2_{n_0} = \sum_i \frac{\left(K_i - C_D V_i n_0^2\right)^2}{\delta K_i^2} \tag{3}$$

with respect to n_0^2, where δK_i is the uncertainty on K_i and $C_D \equiv 0.82\ 10^{-14}/4\pi D_A^2 (1+z)^2$.

2.3.2. Temperature Profile, $kT(r)$

To compute the temperature profiles, we again construct radial bins and fit their spectra, resulting in a projected temperature profile. We then deproject the above temperature profile, using methods similar to those used to deproject the density profile. We choose the size of the radial bins in order to include the lowest number of counts necessary for a temperature determination, with 10% uncertainty. This count number, $N_{\rm nec}$, which is a function of temperature and background count fraction, is estimated by simulating spectra of different total counts, temperatures, and background fractions, $f_{\rm bg}$, to find the necessary counts for a 10% uncertainty on temperature (Elkholy 2012). We find that $N_{\rm nec}$ can approximately be fit by

$$N_{\rm nec}\left(kT, f_{\rm bg}\right) = 500 \times 10^{1.976 f_{\rm bg}} \times \left(\frac{kT}{2\ {\rm keV}}\right)^{1.7}. \tag{4}$$

We extract spectra of at least $N_{\rm nec}$ counts and fit their spectra to an absorbed APEC model in CIAO's tool, *Sherpa*. We create a spectrum from each observation that partially or wholly covers the annulus corresponding to a radial bin, and we simultaneously fit these spectra. We link the temperatures and metal abundances of these spectra across the multiple observations during the fit. Normalizations are only linked for spectra that cover more than 95% of the solid angle of the annular region. Metallicity is left as a free parameter, and the hydrogen column density, n_H, is fixed to the values from the LAB data set of Kalberla et al. (2005). We also include in our online data set the results of analysis with Dickey & Lockman (1990) n_H measurements. We find that leaving n_H as a free parameter returns unreasonable best-fit values on both n_H and temperature. However, for Abell 478, which is reported to have varying n_H by Vikhlinin et al. (2005), we allow n_H to be free, with a minimum equal to the 21 cm measured value.

The background spectrum is extracted from the *Chandra* blank-sky data sets and from source-free regions around cluster observations. The background is modeled as particle background plus X-ray background. The X-ray background is modeled as an absorbed 0.2 keV APEC model, with $n_H = 2.09 \times 10^{22}\ {\rm cm}^{-2}$ and an absorbed power-law component for the cosmic X-ray background, with index set to −1.4. These components are convolved with the instrument response for each CCD chip. The particle background is modeled as a series of Gaussian, exponential, and power-law functions to phenomenologically fit the remaining components of the blank-sky data sets. It is not convolved with the instrument response. The overall background spectral model varies from epoch to epoch and also depends on the CCD chip used.

We assume that the shape of the instrumental background component of the cluster observation is the same as the best-fit model from the corresponding blank-sky data set and compute its normalization as suggested in Maxim Markevitch's cookbook for treating the background data.[7] The overall normalization of the instrumental background is computed by scaling the background normalization according to the ratio of counts in the 9.5–12 keV energy range, in the cluster data set relative to the blank-sky data set. In this manner we attempt to capture any possible change in the background normalization between different epochs. We note that data sets in our sample with OBSID between 7686 and 7701 are missing high-energy counts. Their instrumental background normalization is thus scaled simply by exposure time and solid angle.

Having used the blank-sky data to constrain the instrumental background components, we proceed to fit the X-ray background from the in-field spectra. The latter are modeled with the same model described above plus an additional APEC component to account for residual cluster emission. The APEC model's temperature is fixed at the temperature measured outside a projected radius of 150 kpc, using an initial simple fit.

The in-field spectra are obtained from annuli centered around the cluster center, covering regions that are visually identified to contain mostly background X-ray counts. For Abell 119 and Abell 3571, the cluster emission covers most of the field of view (FOV). We thus rely on the blank-sky background data to model both instrumental and X-ray background components - for these two clusters.

We use CSTAT as our fit statistic, as it is more suitable for energy bins with low counts, where the more commonly used χ^2 statistic introduces bias. After obtaining the best-fit temperature, we compute its uncertainty using *Sherpa*'s `proj()` function, which varies temperature along a grid and searches for the best fit at each temperature by varying the other thawed parameters.

The spectral fitting described above returns a best-fit *projected* temperature for a given radial bin: because the ICM is thought to be optically thin, the emission at one point on the sky is the sum of all emissions from the LOS behind that point. Thus, to compute the true three-dimensional temperature profile, we assume a flexible analytic form for $kT(r)$, vary its parameters repeatedly, projecting it along the LOS in each iteration until the best match is found with the measured projected temperature radial profile. This fitting process is again run using *Sherpa*. The projection is computed according to the prescription in Mazzotta et al. (2004), who show that to recover a single-temperature fit from a mixture of many temperature components one should average these temperatures with a weighting proportional to $n^2 V T^{\alpha}$, where V is the volume of the region of emission. We choose $\alpha = -0.75$, as suggested by the range of values found by Mazzotta et al.

---

[7] http://cxc.harvard.edu/contrib/maxim/acisbg/COOKBOOK

(2004) for spectra of different metallicities. The three-dimensional temperature profile is modeled as in Vikhlinin et al. (2006):

$$kT(r) = kT_0 \frac{(r/r_t)^{-a}}{\left[1 + (r/r_t)^b\right]^{c/b}} \frac{x + T_{\min}/T_0}{x + 1}, \tag{5}$$

where $x = (r/r_{\rm cool})^{a_{\rm cool}}$ and where T_0, r_t, a, b, c, $T_{\min}$, $r_{\rm cool}$, and $a_{\rm cool}$ are fit parameters. The number of free parameters depends on the number of available temperature measurements.

Computing $kT(r)$ and $n_e(r)$ gives us the necessary quantities to measure R_{500}, the gas mass within R_{500}, which we call $M_{\rm gas}$, and the total gravitational mass within the same radius, M_{500}. As described in Elkholy (2012), we do so using an iterative scheme because the three quantities are related. We use the $M - Y_X$ relation of Kravtsov et al. (2006) to relate M_{500} to our measurables, as $Y_X \equiv kT_X M_{\rm gas}$, where kT_X is the temperature measured in the aperture $0.15 < r < 1.0 R_{500}$.

2.3.3. *Uncertainties*

The uncertainties in the entropy profile of each cluster are estimated by generating a set of $S(r)$ models, which are allowed by the data and their uncertainties, as described here. For temperature radial profiles, using the temperature measurements in each radial bin and their error estimate, we randomly generate new "fake" data sets and fit them one at a time. To generate a fake temperature measurement for each radial bin, we draw its value from a random distribution designed to capture the asymmetric uncertainties obtained on the bin's best-fit temperature. This probability distribution is a piece-wise function of two Gaussian distributions on either side of the best-fit temperature, with the standard deviations equal to the measured 1σ upper and lower uncertainties. The latter are not in general equal to each other. Once a complete radial temperature profile is generated over the entire available radial range, we fit it with the same model in Equation (5) and repeat this analysis for 400 iterations.

The same analysis is repeated for the density profiles, where SB measurements are similarly perturbed for 300 iterations according to their uncertainties. The uncertainties in this case are assumed to be symmetric, and the fake SB measurements are drawn from a Gaussian distribution.

To compute the uncertainty on the entropy profile, we compute a set of entropy profiles from pairing different temperature and density profiles from the above generated sets. We iterate through all 400 temperature profiles. For each temperature profile, we iterate through 10 density profiles, computing a temperature profile $S(r) = kT(r)/n_e(r)^{2/3}$ in each iteration. We ensure to choose different density profiles, from one temperature profile to the next, until all 300 profiles are used, at which point we start from the beginning of the density profiles list. The result is an ensemble of 4,000 entropy profiles, which we use to find the distribution of entropy values at any given radius.

2.3.4. *Metallicity Profile Calculation Method*

To compute the metallicity profiles, we take an approach similar to that used to make the temperature profiles. First, using simulated spectra, we estimate the minimum necessary counts, $N^Z_{\rm nec}(kT, Z, f_{\rm bg})$, to obtain a 20% uncertainty on the best-fit metallicity. In this case, $N^Z_{\rm nec}(kT, Z, f_{\rm bg})$ does not have a simple analytical form as does its counterpart for temperature measurement, but rather it is estimated from a weighted average of $N^Z_{\rm nec}$ values estimated for the kT, Z, and $f_{\rm bg}$ values that were simulated (Elkholy 2012). Then, using the derived $N^Z_{\rm nec}$, we extract spectra in radial bins using the same bins used for the $kT(r)$ profile calculation, joining them whenever more counts are needed for a 20% uncertainty temperature estimate. We take the maximum radius of extraction to be R_{500}.

For spectral fitting, we again model both source emissions from the ICM and background. For the background spectra, we use the same best-fit parameters found in the $kT(r)$ analysis above. The background normalization is computed using the same method as in the $kT(r)$ analysis, described in Section 2.3.2. Cluster emission is modeled using a one-temperature model and using a two-temperature model, where the cooler component's temperature is set to one-half of the value of the hotter component's temperature.

We compute the uncertainty on the metallicity in each bin using *Sherpa*'s `proj()` function. From the obtained metallicity profile, we characterize the metallicity of each cluster by two global quantities, $\bar{Z}_{\rm mid}$ and $\bar{Z}_{\rm in}$. We define

$$\bar{Z}_{\rm mid} = \frac{\sum_{0.15 < r_i < 0.3 R_{500}} Z_i M_{{\rm gas},i}}{\sum_{0.15 < r_i < 0.3 R_{500}} M_{{\rm gas},i}}, \tag{6}$$

which is the gas-mass-weighted metallicity over all shells in the range $0.15 < r < 0.3 R_{500}$. Here, Z_i and $M_{{\rm gas},i}$ are, respectively, the metallicity and the gas mass in the ith radial bin. In other words, $\bar{Z}_{\rm mid}$ traces the total iron mass, $M^{\rm mid}_{\rm Fe}$, in the region $0.15 R_{500} < r < 0.3 R_{500}$, according to

$$M^{\rm mid}_{\rm Fe} = A_{\rm Fe} \bar{Z}_{\rm mid} M^{\rm mid}_{\rm gas}, \tag{7}$$

where $A_{\rm Fe} = 0.0019$ is the solar abundance of iron by mass, according to the photospheric measurements in Anders & Grevesse (1989) that were assumed for our spectral analysis, and $M^{\rm mid}_{\rm gas}$ is the gas mass contained in the same region. Similarly,

$$\bar{Z}_{\rm in} = \frac{\sum_{r_i < 0.15 R_{500}} Z_i M_{{\rm gas},i}}{\sum_{r_i < 0.15 R_{500}} M_{{\rm gas},i}}. \tag{8}$$

Hereafter, $\bar{Z}_{\rm mid}$ will be used as a measure of the metallicity of the bulk of a cluster, and $\bar{Z}_{\rm in}$ will be used as a measure of the core metallicity in clusters.

3. RESULTS

We make our data available on the FTP site.[8] ftp://space.mit.edu/pub/tamer/ebc2015/

Appendix A contains the plot of the entropy profile for each cluster, and the individual metallicity radial profiles are shown in Appendix B.

We first note that four clusters of our sample deviate considerably from spherical symmetry simply based on their SB image. These clusters, Abell 754, Abell 2256, Abell 3376, and Abell 3667, are known to be undergoing merging events. We exclude the disturbed clusters from our analysis, except when noted.

---

[8] The file named "README" within this FTP site details the content of the data.

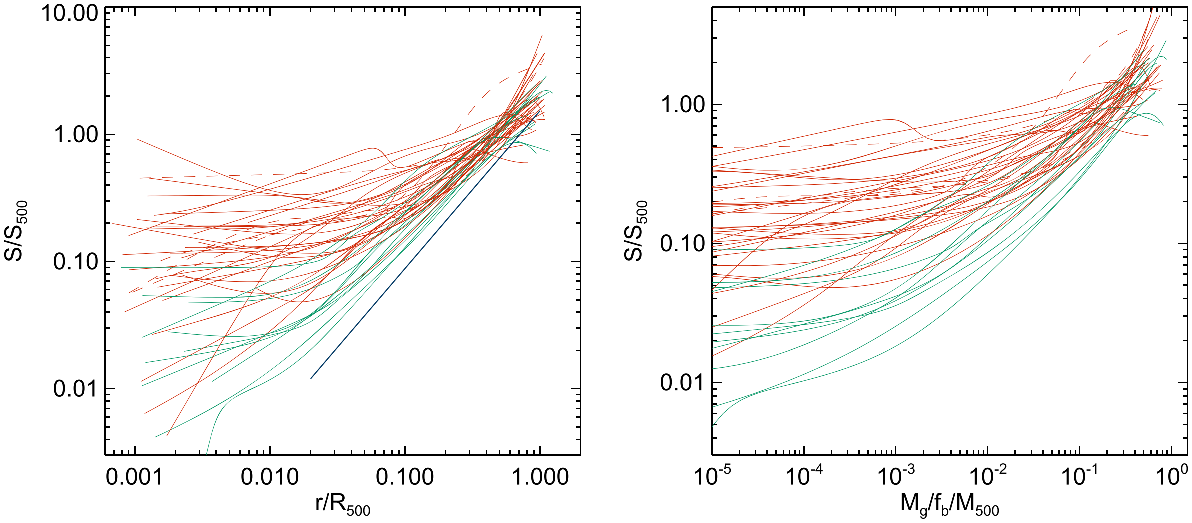

Figure 1. Plot of all computed entropy profiles. Left: scaled entropy, S/S_{500}, as a function of scaled radius, r/R_{500}. Right: scaled entropy as a function of enclosed gas mass fraction, F_g. Turquoise curves are for CC clusters, and red curves are for NCC clusters. The dark-blue curve is the power law describing the Voit 2005 entropy profile found in hydrodynamical simulations. The dashed curves are for the four morphologically disturbed clusters Abell 754, Abell 2256, Abell 3376, and Abell 3667.

Table 6 in Appendix C shows the measured values of kT_X, R_{500}, M_{500}, and $M_{\rm gas}$ for each cluster.

3.1. Entropy Profiles

Our best-fit results for density and temperature radial profiles are shown in Tables 7 and 8, respectively, in Appendix D.

We overplot the computed entropy profiles for all of our sample's clusters in Figure 1. On the left panel, we plot entropy as a function of radius, which we normalize with respect to R_{500}. On the right panel, we plot entropy as a function of enclosed gas mass fraction, $F_g \equiv M_g/(f_b M_{500})$, where M_g is the interior gas mass, and f_b the universal baryon fraction with respect to all matter, i.e., $f_b = \Omega_b/\Omega_m$. We use F_g to plot entropy profiles because this is the variable used in a Lagrangian description of the entropy distribution in clusters (see, e.g., Tozzi & Norman 2001; Voit et al. 2003; Nath & Majumdar 2011). The entropy in both panels is normalized with respect to S_{500} (Voit et al. 2003), the characteristic entropy of the cluster at R_{500}:

$$S_{500} \equiv \frac{GM_{500}\mu m_p}{2R_{500}\left[500 f_b\,\rho_c\left(z\right)/\mu_e m_p\right]^{2/3}}, \tag{9}$$

where μ and μ_e are the mean number of nucleons per particle and per electron, respectively, m_p is the proton mass, and $\rho_c(z)$ is the universe's critical density at the redshift of observation, z. The characteristic entropy, S_{500} at an overdensity $\delta = 500$, is simply the entropy obtained using the characteristic temperature at $\delta = 500$, which is the equivalent of the virial temperature but defined for R_{500} instead of the virial radius:

$$kT_{500} \equiv \frac{GM_{500}\mu m_p}{2R_{500}}, \tag{10}$$

and using the average electron density inside R_{500}

$$\bar{n}_e = 500 f_b\,\rho_c(z)/\mu_e m_p. \tag{11}$$

It represents the entropy scale set by gravity in the self-similar picture.

The dark-blue line in Figure 1 represents a model of the entropy profile of a cluster generated from gravitational collapse alone, which was calculated with hydrodynamical adaptive-mesh refinement (AMR) simulations in Voit et al. (2005). Voit's entropy profile is approximated analytically as a power law as

$$S_V(r) = 1.53 S_{500}\left(\frac{r}{R_{500}}\right)^{1.24}, \tag{12}$$

and is valid for radii larger than approximately $0.2R_{500}$. We employ the conversion used in Pointecouteau et al. (2005) to express Equation (12) in terms of S_{500} and R_{500}, as opposed to the measurements at an overdensity of 200, presented in Voit et al. (2005).

The turquoise curves in Figure 1 represent cool core clusters (CC), and the red curves are for noncool core clusters (NCC). We use the SB concentration, $c_{\rm SB}$, introduced in Santos et al. (2008) to quantify the cool core state of a cluster. The parameter $c_{\rm SB}$ is defined as the ratio of the SB within 40 kpc to that within 400 kpc of the *peak* of the emission.[9] The values of $c_{\rm SB}$ are shown in Table 9. We define CC clusters as clusters with $c_{\rm SB} > 11$, and NCC clusters have $c_{\rm SB} < 11$.

The first observation to make is that for most of the studied radial range, all entropy profiles lie above the Voit et al. (2005) gravitationally induced entropy model. This result has been known in the literature (e.g., Ponman et al. 1999; Pratt et al. 2010), and the additional entropy in the observations has been attributed to nongravitational processes, such as winds and AGN heating. Second, some of the entropy profiles in Figure 1 show a decrease or a flattening starting at a radius between 0.3 and $0.8R_{500}$. This is due to a decrease in measured temperature toward the outskirts of many clusters, which is not matched by a steep-enough decrease of measured density with

---

[9] For calculating $c_{\rm SB}$, we use the emission peak as the cluster center, unlike in previous analysis where the emission is used instead.

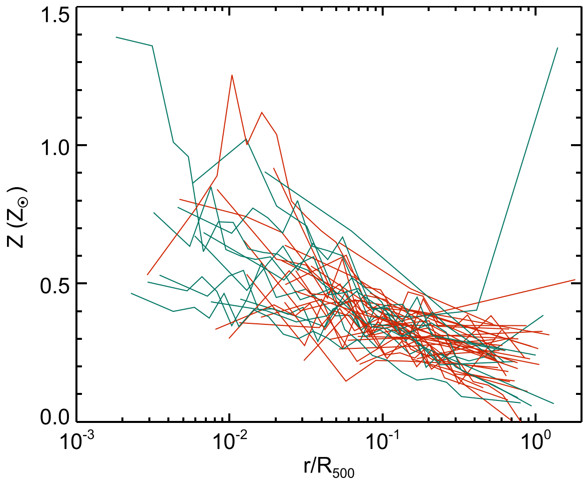

Figure 2. Superimposed metallicity profiles of clusters. Red curves are for NCC clusters, and turquoise curves are for CC clusters.

radius. Such a configuration of large amounts of lower-entropy gas at larger radii is not physically stable. There are two sources of systematic error that can be contributing here to give erroneous temperature and density measurements. First, the systematics in our estimate of the level of X-ray background will translate into an error in the estimate of the cluster SB at these large radii, introducing a bias to the inferred density and also biasing outer temperature estimates. Second, the deprojection method of Mazzotta et al. (2004), which we employ to deproject the measured two-dimensional temperature profile to a three-dimensional $kT(r)$, is known to be less accurate when there is a significant contribution to the emission from spectral components with temperatures smaller than ~3 keV (Mazzotta et al. 2004; Vikhlinin 2006).

In addition, we show in Figure 14, in Appendix A, the individual entropy profiles we compute. The estimate of the 1σ range of entropy at each radius is represented by the turquoise-shaded region. The uncertainty in the measured temperatures, which translates into an uncertainty in the parameters of the temperature radial profile, is the main contributor to the uncertainty in the entropy profile. By comparison, the contribution of the density uncertainty to the entropy uncertainty is much smaller.

The light-gray error bars, in Figure 14, represent the entropy profiles measured in the ACCEPT study by Cavagnolo et al. (2009). Our entropy profiles agree, in general, with the ACCEPT entropy profiles, where they overlap. However, we extend our entropy profiles to larger radii, where we model both density and temperature.

3.2. *Metallicity Profiles and Global Measurements*

3.2.1. *Profiles*

We overplot all obtained metallicity profiles in Figure 2. The dispersion in the values of observed cluster metallicities decreases for radii larger than $0.1-0.2R_{500}$, despite the larger uncertainty associated with measured metallicities at these high radii. One metallicity measurement seems to be exceptionally larger at large radius, as seen in Figure 2. This is the last metallicity measurement for Abell 2204, where the modeling of the background is likely suffering from systematics, despite an acceptable fit statistic. The outermost spectra for Abell 2204 are found to have excess low-energy counts, which are mostly fit by our galactic X-ray background component.

We also present in Appendix B plots of our measured metallicity profiles, individually, with their estimated uncertainty. The two vertical lines in Figure 15 are drawn at radii $0.15R_{500}$ and R_{500}, for those clusters where we can measure M_{500} and R_{500} using our iterative method.

3.2.2. *Core Metallicity, $\bar{Z}_{\rm in}$*

The measured values of $\bar{Z}_{\rm in}$ are shown in Table 10, in Appendix F. We plot $\bar{Z}_{\rm in}$ as a function of cluster mass and as a function of the global temperature measurement, kT_X, in Figure 3. Figure 3 suggests that low-mass clusters ($M_{500} < 3.5 \times 10^{14}\,M_\odot$) exhibit more dispersion in $\bar{Z}_{\rm in}$ than high-mass clusters do.

To quantify this latter observation, we show in Table 2 the error-weighted mean and the standard deviation of the values of $\bar{Z}_{\rm in}$, for clusters grouped by mass. The results for the one-temperature fit are labeled "1T," and those for the two-temperature fit "2T." The standard deviation of $\bar{Z}_{\rm in}$ for clusters with $M_{500} > 3.5 \times 10^{14}\,M_\odot$ is 2.4–2.9 times smaller than that for clusters with $M_{500} < 3.5 \times 10^{14}\,M_\odot$, for the 1T and the 2T models, respectively. The value of χ^2 for each subset shows whether the dispersion for low-mass clusters is solely the result of measurement uncertainties. Here

$$\chi^2 = \sum_i \frac{\left(\bar{Z}_{{\rm in},i} - \left\langle \bar{Z}_{\rm in} \right\rangle\right)^2}{\delta \bar{Z}^2_{{\rm in},i}}, \tag{13}$$

where the sum is over the sample of clusters denoted by i, $\bar{Z}_{{\rm in},i}$ is the ith cluster's central metallicity, $\delta \bar{Z}_{{\rm in},i}$ is its uncertainty, and $\langle \bar{Z}_{\rm in} \rangle$ the sample mean.

For low-mass clusters, we find that χ^2 is more than 30 times the number of degrees of freedom (dof) for both the 1T and 2T fits. This confirms that the dispersion seen in low-mass clusters —in the range $(0.12–0.15)Z_\odot$—is not driven by measurement uncertainties. On the contrary, the dispersion of $\bar{Z}_{\rm in}$ in high-mass clusters has a more significant contribution from measurement uncertainties, despite being much smaller at $\sim 0.05\,Z_\odot$.

The above results are unchanged when we include the $\bar{Z}_{\rm in}$ measurements from the high-mass, asymmetrical clusters Abell 754, Abell 2256, and Abell 3667, which have $\bar{Z}_{\rm in} = 0.369^{+0.036}_{-0.035}$, $0.389^{+0.065}_{-0.061}$, and $0.345^{+0.012}_{-0.011} Z_\odot$, respectively. These clusters were excluded from the above analysis based on their asymmetric morphologies. The 1T dispersion of $\bar{Z}_{\rm in}$ over the high-mass subset decreases to $0.047Z_\odot$ when the above three clusters are included, while the 2T dispersion does not change significantly.

To emphasize the difference between low- and high-mass cluster metallicity dispersions, we show in Figure 4 the superimposed metallicity radial profiles of all clusters in our sample, where we differentiate between the two subsets by color. Green data points represent low-mass clusters, and orange data points represent larger clusters. We can see in this plot that the metallicity profiles of the large clusters are less scattered than those of the low-mass clusters. This translates into the different observed dispersions of $\bar{Z}_{\rm in}$ seen in Figure 3.

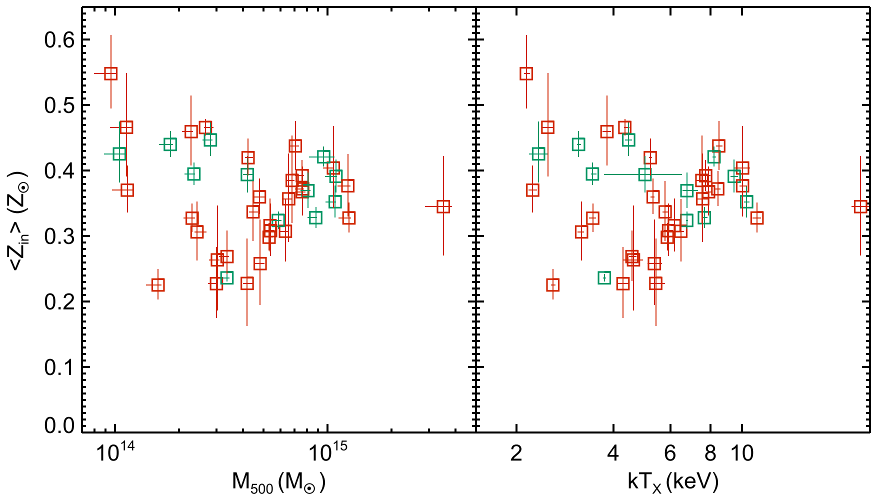

Figure 3. Core metallicity as a function of cluster mass or temperature. Left: $\bar{Z}_{\rm in}$ versus M_{500}. Right: $\bar{Z}_{\rm in}$ versus kT_X. Red points are for NCC clusters, and turquoise points are for CC clusters.

Table 2
Statistics for $\bar{Z}_{\rm in}$

	Model	Mean ($Z_\odot$)	Std. Dev. ($Z_\odot$)	χ^2/dof
$M_{500} < 3.5 \times 10^{14}\,M_\odot$	1T	0.30	0.12	33. (490./15)
	2T	0.25	0.15	31. (470./15)
$M_{500} > 3.5 \times 10^{14}\,M_\odot$	1T	0.36	0.050	2.6 (64./25)
	2T	0.35	0.052	1.2 (29./25)

Note. Error-weighted mean, standard deviation of $\bar{Z}_{\rm in}$ and χ^2/dof with respect to calculated mean. Results are shown for clusters with M_{500} smaller than and larger than $3.5 \times 10^{14}\,M_\odot$ and for fits using the 1T and the 2T spectral models.

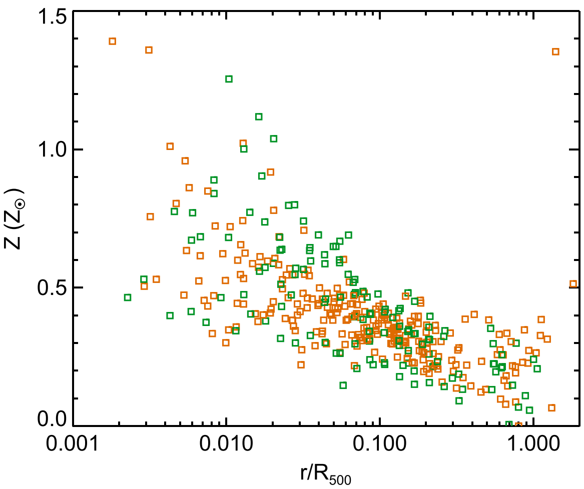

Figure 4. Superimposed metallicity profiles of clusters. Orange data points are for clusters with mass $M_{500} > 3.5 \times 10^{14}\,M_\odot$, and green data points correspond to clusters with $M_{500} < 3.5 \times 10^{14}\,M_\odot$.

Comparing CC and NCC clusters, we find that for CC clusters $\bar{Z}_{\rm in} = 0.30 \pm 0.10 Z_\odot$, while for NCC clusters $\bar{Z}_{\rm in} = 0.37 \pm 0.080 Z_\odot$. We find that $\bar{Z}_{\rm in}$ is larger for NCC clusters than for CC clusters in this sample, despite the difference being within the measured dispersions of both quantities. This contrasts with the metal excess measured in the centers of CC clusters in, e.g., De Grandi & Molendi (2001).

3.2.3. *Outer Metallicity, $\bar{Z}_{\rm mid}$*

The measured values of $\bar{Z}_{\rm mid}$ are shown in Table 10, in Appendix F. In Figure 5, we show a plot of $\bar{Z}_{\rm mid}$, which measures the average metallicity outside the core, as a function of the total mass, M_{500}, and as a function of kT_X. In Table 3, we show the statistics for the distribution of $\bar{Z}_{\rm mid}$ values. In the case of outer metallicity, we no longer detect a clear difference in the dispersions of high- and low-mass clusters. However, when we compare $\bar{Z}_{\rm mid}$ to $\bar{Z}_{\rm in}$, we find that for each of the low- and high-mass cluster samples, $\bar{Z}_{\rm mid}$ values are smaller than $\bar{Z}_{\rm in}$ values. For high-mass clusters, for example, the mean and standard deviation for $\bar{Z}_{\rm mid}$ are $(0.27 \pm 0.073) Z_\odot$, while for $\bar{Z}_{\rm in}$ they are $(0.36 \pm 0.050) Z_\odot$. This points to a decrease in the iron mass fraction as we move from the core region, $r < 0.15 R_{500}$, to the outer region, $0.15 < r < 0.3 R_{500}$. This decrease is however within the measured dispersions of $\bar{Z}_{\rm mid}$ and $\bar{Z}_{\rm in}$ and is also found for low-mass clusters.

3.3. *Metallicity–Entropy Relation*

One direct approach to looking for a relation between pre-enrichment and preheating is to look for a correlation between the ICM nongravitational entropy and the ICM bulk metallicity measured outside the central region of the cluster, $\bar{Z}_{\rm mid}$. In addition, we also consider the relation between nongravitational entropy and $\bar{Z}_{\rm in}$. We use the ratio of measured entropy to the expected gravitational entropy, $S_{\rm grav}$, to probe the amount of nongravitational entropy. We define the scaled entropy $x_s \equiv S/S_{\rm grav}$, which we use as a measure for any nongravitational entropy, and discuss our assumptions on $S_{\rm grav}$ below.

The metallicity–entropy relation is studied with entropy measured at several locations in the clusters. First, we consider entropy measurements at fixed R_{500}-scaled radii. This is justified because the gravitational entropy model of Voit et al. (2005) scales self-similarly and is given in terms of a profile that is a function of r/R_{500}. In this case, we define $S_{\rm grav}$ as the expected gravitational entropy from Voit's model, $S_{\rm grav}(r) = S_V(r)$. Second, we take a Lagrangian approach and study entropy at a fixed interior gas mass fraction, $F_g \equiv M_g/(f_b M_{500})$, where M_g is the interior gas mass (see, e.g., Tozzi & Norman 2001; Voit et al. 2003; Nath & Majumdar 2011). This can be useful because buoyancy tends

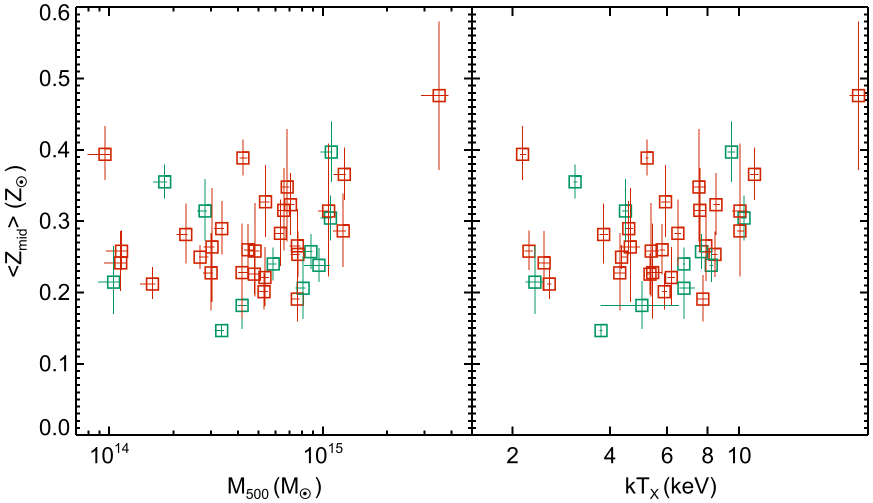

Figure 5. Outer metallicity as a function of cluster mass or temperature. Left: $\bar{Z}_{\mathrm{mid}}$ versus M_{500}. Right: $\bar{Z}_{\mathrm{mid}}$ versus kT_X. Red points are for NCC clusters, and turquoise points are for CC clusters.

Table 3
Statistics for $\bar{Z}_{\mathrm{mid}}$

	Model	Mean ($Z_\odot$)	Std. Dev. ($Z_\odot$)	χ^2/dof
$M_{500} < 3.5 \times 10^{14}\, M_\odot$	1T	0.22	0.079	10. (150./15)
	2T	0.20	0.085	9.1 (140./15)
$M_{500} > 3.5 \times 10^{14}\, M_\odot$	1T	0.27	0.073	3.2 (79./25)
	2T	0.27	0.074	2.3 (56./25)

Note. Error-weighted mean, standard deviation of $\bar{Z}_{\mathrm{mid}}$ and χ^2/dof with respect to calculated mean. Results shown for clusters with M_{500} smaller than and larger than $3.5 \times 10^{14}\, M_\odot$, and for fits using the 1T and the 2T spectral models.

to order the ICM such that low-entropy gas finds its way to the bottom of the cluster potential, while high-entropy gas rises to large radii. In this latter case, we simply use $S_{\mathrm{grav}} = S_{500}$ to scale the entropy, to avoid using a specific model of entropy dependence on F_g, while still capturing the S_{500} scaling expected in self-similar galaxy clusters.

In the analysis below, not all clusters are included for each measurement. The first filter we apply is to exclude four clusters that are visually judged to greatly deviate from spherical symmetry. These are Abell 754, Abell 2256, Abell 3376, and Abell 3667. In addition, in the successive measurements at different radii, below, we only include a cluster at a certain radius if the size of the FOV is larger than the radius of interest.

We start by looking at the $\bar{Z}_{\mathrm{mid}} - x_s$ relation at a constant scaled radius. As described above, in this case, $x_s = x_s(r) = S(r)/S_{\mathrm{grav}}(r) = S(r)/S_V(r)$. We measure entropy at $r = 0.2R_{500}$, $0.3R_{500}$, $0.5R_{500}$, $0.8R_{500}$, and $1R_{500}$. Our measurements are shown in Figure 6. Similarly, we consider the same relation at fixed F_g. We choose values of F_g corresponding to the sample average across all clusters, at $r = 0.2$, 0.3, 0.5, 0.8, and 1 R_{500}. Table 4 shows the correspondence between scaled radius and the sample average gas mass fraction. Our metallicity–entropy measurements at constant F_g are shown in Figure 7.

As can be seen in Figures 6 and 7, there is no visible correlation between our estimate of nongravitational entropy and the bulk metal content of a cluster, as estimated by $\bar{Z}_{\mathrm{mid}}$.

As for metallicity measured in the core, $\bar{Z}_{\mathrm{in}}$, we expect low-radius metallicity measurements to probe processes that occur after the collapse of the cluster. We repeat the analysis performed above, with $\bar{Z}_{\mathrm{in}}$ instead of $\bar{Z}_{\mathrm{mid}}$. Figure 8 shows plots of the measured inner metallicity, $\bar{Z}_{\mathrm{in}}$, against the ratio of measured entropy to S_V, at the above-mentioned scaled radii. Again, there is only a weak indication of a correlation between inner metallicity and x_s at smaller radii. We perform a statistical analysis using a bootstrap resampling method to calculate the significance of the correlation between the various metallicity and entropy measures. The lowest obtained p-values are of 1.3 and 2.0% for the CC-only samples at $r = 0.3$ and $0.2R_{500}$, respectively. Figure 9 also shows the $\bar{Z}_{\mathrm{in}}$–x_s plot, this time for x_s measured at constant F_g.

4. DISCUSSION

4.1. Inner Metallicity Scatter Systematics

As was presented in Section 3.2.2, the core iron mass fraction, $\bar{Z}_{\mathrm{in}}$, over our cluster sample has a different distribution for low-mass clusters than for high-mass clusters. Measurements of $\bar{Z}_{\mathrm{in}}$ in large clusters $(M > 3.5 \times 10^{14}\, M_\odot)$ are narrowly distributed around their mean of $0.36Z_\odot$, with a standard deviation of only $\sigma_Z = 0.050Z_\odot$. On the other hand, $\bar{Z}_{\mathrm{in}}$ for low-mass clusters has a standard deviation of $\sigma_Z = 0.12Z_\odot$, around a slightly lower mean value for the sample. See Table 2 for details. The uncertainties on the individual $\bar{Z}_{\mathrm{in}}$ measurements are too small to explain the dispersion in low-mass clusters because $\chi^2/\mathrm{dof} = 33$. This means that the observed scatter is intrinsic to the data and not a result of measurement uncertainties. On the other hand, we calculate $\chi^2/\mathrm{dof} = 2.6$ for $\bar{Z}_{\mathrm{in}}$ in large clusters, indicating that measurement uncertainties contribute relatively more to the scatter, which nonetheless has a much lower value of only $\sigma_Z = 0.050Z_\odot$.

We attempt here to understand the difference between the distribution of inner metallicity values for low- and high-mass clusters. First we check whether the observed effect is due to systematics, and then we present several physical explanations of the measurements in the following sections.

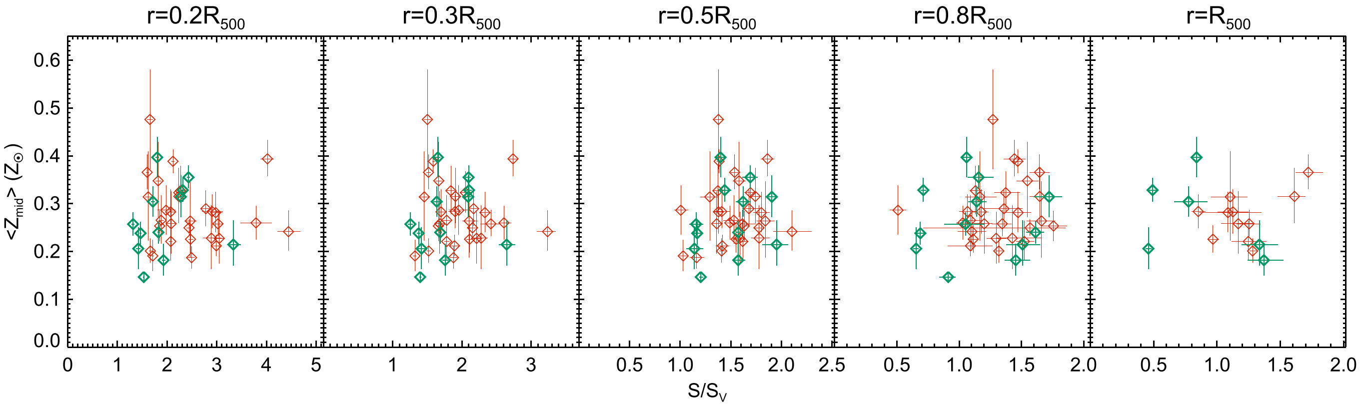

Figure 6. Plot of gas-mass-weighted metallicity, $\bar{Z}_{\text{mid}}$, versus the scaled entropy, S/S_V. Panels from left to right represent the cases where entropy is measured at $r = 0.2R_{500}$, $r = 0.3R_{500}$, $r = 0.5R_{500}$, $r = 0.8R_{500}$, and $r = R_{500}$. Only clusters with *Chandra* coverage at each of these radii are represented in the corresponding panel. Turquoise data points are for CC clusters, and red points represent NCC clusters. Abell 400 is the outlying cluster with large metallicity at $\bar{Z}_{\text{mid}} \sim 0.6Z_{\odot}$.

Table 4
Cluster Sample Average of F_g at Various Radii

r/R_{500}	0.2	0.3	0.5	0.8	1.0
F_g	0.050	0.10	0.24	0.47	0.63

The first systematic effect to be tested concerns the inclusion of X-ray photons from the region $r > 0.15R_{500}$ in the computation of $\bar{Z}_{\text{in}}$. This occurs because spectral regions for metallicity measurement are defined before R_{500} is computed, while we desire for $\bar{Z}_{\text{in}}$ to measure the metallicity within $0.15R_{500}$. Once R_{500} is calculated, to compute $\bar{Z}_{\text{in}}$, we include all radial bins that overlap the disk $r < 0.15R_{500}$. The last such bin will, in general, extend beyond $r = 0.15R_{500}$. We address this by estimating the fraction of counts originating from the region $r > 0.15R_{500}$, which are used to compute $\bar{Z}_{\text{in}}$. We denote this count fraction by f_{out} and show a histogram of its distribution in our sample in Figure 10.

Because metallicity profiles generally decrease with radius, including emission from large radii for a given cluster might bias its $\bar{Z}_{\text{in}}$ measurement, compared to the rest of the sample. We would like to test the magnitude of this effect. We thus repeat the measurement of $\bar{Z}_{\text{in}}$ dispersion with a sample that excludes clusters with a significant contribution from $r > 0.15R_{500}$. We choose the cutoff value to be $f_{\text{out}} = 0.25$ to capture the peak of the distribution of clusters with $f_{\text{out}} < 0.25$ seen in Figure 10. We calculate the mean, dispersion, and χ^2/dof statistics as was done with the complete sample. The results are displayed in Table 5. We find that the difference between the high- and low-mass cluster samples still remains for dispersion and χ^2/dof. We thus conclude that the spectral bin sizes do not have a large effect on this discrepancy in measured metallicity dispersions.

The second systematic effect we test is the effect of the number of radial bins used to measure $\bar{Z}_{\text{in}}$ in the obtained value. As can be seen in Equation (8), $\bar{Z}_{\text{in}}$ is a weighted sum of single metallicity measurements. For clusters without enough photons to create multiple radial bins within $0.15R_{500}$, the measurements will give less precise estimates of $\bar{Z}_{\text{in}}$, on average. We find, however, that there is no significant dependence of $\bar{Z}_{\text{in}}$ on the number of bins used to estimate it. In addition, we also find that the number of bins covering $r < 0.15R_{500}$ does not depend on M_{500}.

We also repeat the analysis using a constant physical radius aperture of 150 kpc to compute the inner iron mass fraction. We find that the different levels of dispersion remain unchanged, even with the physical radius aperture.

4.2. *Metallicity Scatter as a Reflection of Structure Formation*

One possible physical explanation for this observed difference between low-mass and high-mass clusters is that the metal content in clusters is driven by the merger history of clusters. In the hierarchical model of structure formation, low-mass clusters, groups, and galaxies merge to form the larger-mass clusters. Thus, if the metal content is nonuniform across all of these progenitors as they merge with each other, the resulting metallicity is an average of the initial progenitor metallicities. In a simple model, if the metallicities of these progenitor structures are distributed around a mean universal value, Z_0, then the total metal content in a cluster formed by the merger of all of these components should approach Z_0 as the number of components increases. The iron mass fraction, $\bar{Z}_{\text{in}}$, of a large cluster will thus be an average of the metallicities of its smaller progenitors.

Under this hypothesis, the decrease of the dispersion of $\bar{Z}_{\text{in}}$ as we go from low-mass clusters to high-mass clusters simply results from the mixing of gas from the low-mass clusters after they merge to make larger clusters. The mixing then results in averaged, less dispersed metallicity values in the merged clusters compared to the initial progenitors' metallicities. It must be noted, however, that a high-mass cluster from our sample, say of $M_{500} \sim 10^{15}\,M_{\odot}$, will not be exclusively formed by the merger of $10^{14}\,M_{\odot}$-sized clusters, i.e., from the low-mass extreme of our sample. A $10^{15}\,M_{\odot}$ cluster will undergo numerous mergers involving galaxy- and group-sized halos, as well as a smooth and continuous accretion (see, e.g., Fakhouri et al. 2010). This does not contradict the above hypothesis because the more numerous the components making up a cluster are, the closer its metallicity approaches the universal average value.

If this is the correct explanation for the observed larger dispersion of $\bar{Z}_{\text{in}}$ in low-mass clusters, then it should also be reflected in the outer radii metallicity, $\bar{Z}_{\text{mid}}$, which is measured in the range $0.15 < r < 0.3R_{500}$. Our analysis however does not detect the same signal in the outer regions as we do for inner metal content. The sample dispersion in $\bar{Z}_{\text{mid}}$ is roughly

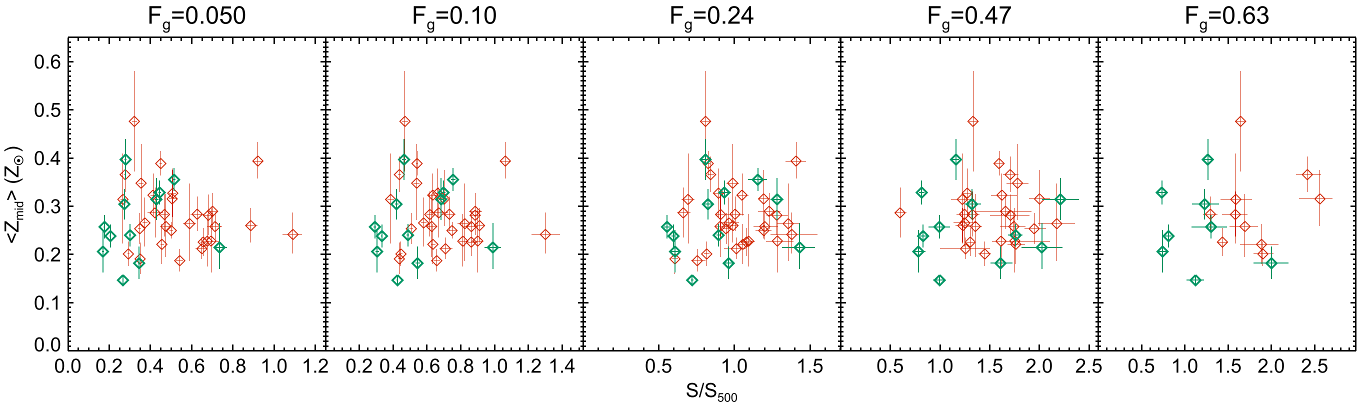

Figure 7. Plot of gas-mass-weighted metallicity, $\bar{Z}_{\rm mid}$, versus the scaled entropy, S/S_V. Panels from left to right represent the cases where entropy is measured at $F_g = 0.050$, $F_g = 0.10$, $F_g = 0.24$, $F_g = 0.47$, and $F_g = 0.63$. Only clusters with *Chandra* coverage at each of these radii are represented in the corresponding panel. Turquoise data points are for CC clusters, while red points represent NCC clusters. Abell 400 is the outlying cluster with large metallicity at $\bar{Z}_{\rm mid} \sim 0.6 Z_\odot$.

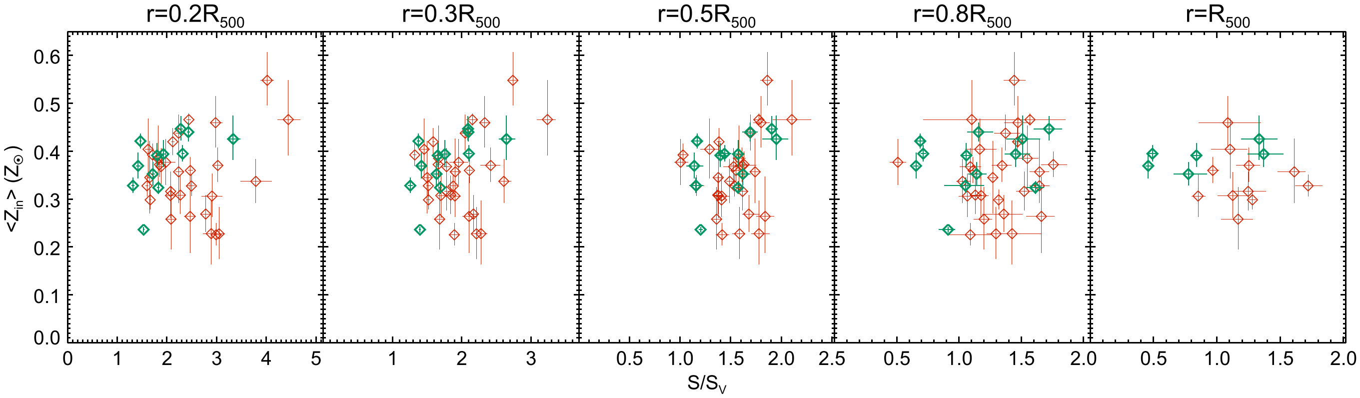

Figure 8. Plot of gas-mass-weighted metallicity, $\bar{Z}_{\rm in}$, versus the scaled entropy, S/S_V. Panels from left to right represent the cases where entropy is measured at $r = 0.2R_{500}$, $r = 0.3R_{500}$, $r = 0.5R_{500}$, $r = 0.8R_{500}$, and $r = R_{500}$. Only clusters with *Chandra* coverage at each of these radii are represented in the corresponding panel. Turquoise data points are for CC clusters, and red points represent NCC clusters.

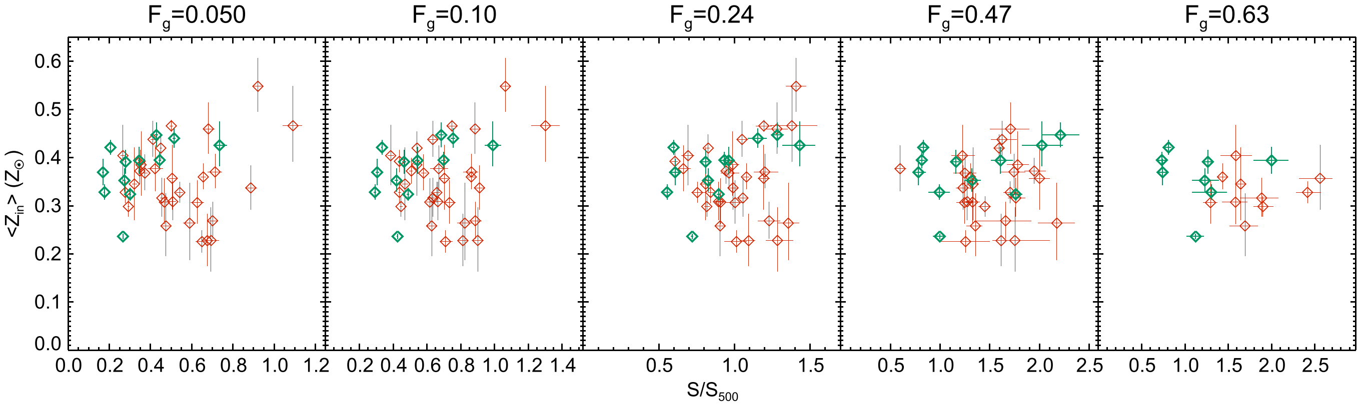

Figure 9. Plot of gas-mass-weighted metallicity, $\bar{Z}_{\rm in}$, versus the scaled entropy, S/S_V. Panels from left to right represent the cases where entropy is measured at $F_g = 0.050$, $F_g = 0.10$, $F_g = 0.24$, $F_g = 0.47$, and $F_g = 0.63$. Only clusters with *Chandra* coverage at each of these radii are represented in the corresponding panel. Turquoise data points are for CC clusters, and red points represent NCC clusters.

$0.079 Z_\odot$ ($0.073 Z_\odot$) for the low-mass (high-mass) sample, and the contribution of measurement uncertainties to that dispersion is estimated to be around $0.04 Z_\odot$ ($0.05 Z_\odot$) for the low-mass (high-mass) sample.

The decrease of the dispersion of *inner* metallicity from small to large clusters requires that, as clusters merge, metals from the progenitor clusters are able to efficiently find their way to the center of the cluster, while avoiding mixing with gas in the outer regions of clusters. Interestingly, the hydrodynamical simulations of Cora (2006) credit the infall of cold metal-rich clumps from large radii for the metal enrichment of the cluster central regions. A similar process is also one of the mechanisms invoked in Million et al. (2011) to explain the existence of a peak in the observed radial profiles of SNCC's metal products, also observed in, e.g., Sanders & Fabian (2006), Simionescu et al. (2008a), and Simionescu et al. (2010). Metal-rich gas from a small cluster, or from a galaxy, merging into a larger one can avoid mixing with the

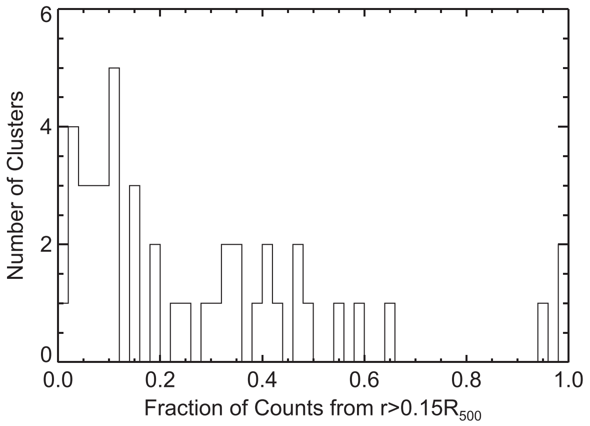

Figure 10. Distribution of the values of f_{out} from the ensemble of $\bar{Z}_{\text{in}}$ measurements. See the text in Section 4.1 for a description of f_{out}.

Table 5
Statistics for $\bar{Z}_{\text{in}}$ Excluding Clusters with $f_{\text{out}} > 0.25$

	Model	Mean ($Z_\odot$)	Std. Dev. ($Z_\odot$)	χ^2/dof
$M_{500} < 3.5 \times 10^{14}\, M_\odot$	1T	0.30	0.15	59. (470./8)
	2T	0.26	0.18	57. (460./8)
$M_{500} > 3.5 \times 10^{14}\, M_\odot$	1T	0.36	0.038	3.7 (49./13)
	2T	0.35	0.043	1.5 (19./13)

Note. Similar to Table 2, using a cluster sample that excludes $f_{\text{out}} > 0.25$ clusters.

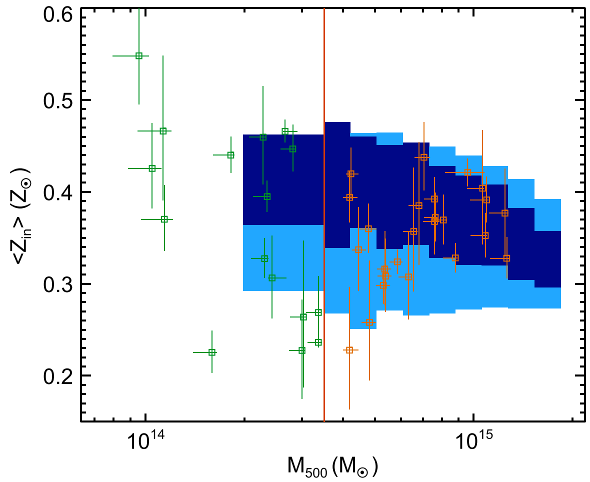

Figure 11. The width of the metallicity distribution, resulting from the hypothetical merger of low-mass clusters from our sample. The light (dark) blue region represents the 95% (68%) spread of generated metallicities. The green and orange data points represent our measurements in low- and high-mass clusters, respectively. The vertical line is plotted at M_{500}=3.5 × $10^{14}\, M_\odot$ and separates the above two samples.

bulk ICM at large radii if its entropy is low enough to allow it to pierce through the outer ICM and reach the center of the cluster. In addition, the absence of this discrepancy in the outer regions of clusters could imply that metals in the outer regions come from a source with a more uniform metallicity level, i.e., a source whose metallicity varies less from cluster to cluster. Such a homogeneous source could be the gas that is accreted very early in the formation of clusters and whose metal contribution is generally referred to as pre-enrichment, which we further discuss in Section 4.3. Along the same lines, a slightly different interpretation of this finding is that, as time goes by, the halos that merge later tend to have a wider distribution of metallicities than those that merge earlier.

The hypothesis that merger statistics is behind the observed metallicity distribution across clusters can be tested in models that combine the statistics of structure formation with metal production in merging halos, using a semianalytical approach. Such a model was built in Elkholy (2012) to test other aspects of cluster chemical and dynamical histories and can be adapted to test whether such observations can be reproduced semianalytically.

We provide here, however, a very crude test of the above hypothesis. We would like to test whether the metallicities of clusters formed through the mergers of low-mass clusters from our sample have a distribution similar to that of the metallicities of our high-mass clusters. To this end, we start by computing the metallicity $\bar{Z}_{\text{in}}$ resulting from the merger of two clusters from the sample of clusters in Figure 3 with $M_{500} < 3.5 \times 10^{14}\, M_\odot$. We draw any two clusters from the low-mass subset and define the metallicity resulting from their merger as the gas-mass-weighted average of the $\bar{Z}_{\text{in}}$ values of the two merging clusters. The gas mass used in weighting the average is that measured within $0.15R_{500}$ from the data. The resulting metallicity is assigned to a mass, M_{500}, that is the sum of the masses of the merging clusters. This is repeated with three-, four-, five-, and six-cluster mergers, again based on our $\bar{Z}_{\text{in}}$ measurements in low-mass clusters. Our generated metallicity distribution thus comes from all possible mergers between six or less clusters from our low-mass cluster sample.

Figure 11 shows the result of the above simulation superimposed on our data points. We recover qualitatively the trend in our data whereby the width of the distribution of cluster metallicities decreases with mass. Beyond this toy model, a model incorporating more detailed statistics of structure formation, as well as a more sophisticated model for metal content in merging clusters, is required to lend support to the hypothesis linking our metallicity measurements to structure formation.

4.3. *Support for Pre-enrichment?*

We argue above that the fact that metallicity dispersion as a function of cluster mass is not observed to change in the outer regions, while it does vary in inner regions, can be explained if, outside the cluster core, most of the metals are the result of pre-enrichment, which is the metallicity level set before cluster formation (e.g., Fujita et al. 2008; Matsushita et al. 2013; Werner et al. 2013). The pre-enriched gas would have an approximately universal metallicity level, compared to the cold infalling halos contributing metals at later times, whose gas metallicity values are more diverse.

We find another clue pointing to this initial pre-enrichment metallicity level—presumed to be the same for all clusters—when we compare $\bar{Z}_{\text{in}}$ values to the stellar-to-gas mass fractions in clusters. Dai et al. (2010) measure the stellar and baryon mass fractions of clusters with temperatures $1 \lesssim kT_X \lesssim 10$ keV, using 2MASS data for optical measurements and *ROSAT* data for X-ray measurements. They measure a decreasing stellar-to-gas mass ratio, r_{sg}, as a function of cluster temperature, kT_X. Using the results of Dai et al. (2010), we can thus estimate the stellar mass from the X-ray temperature of a cluster and test whether it correlates with the metallicity of the

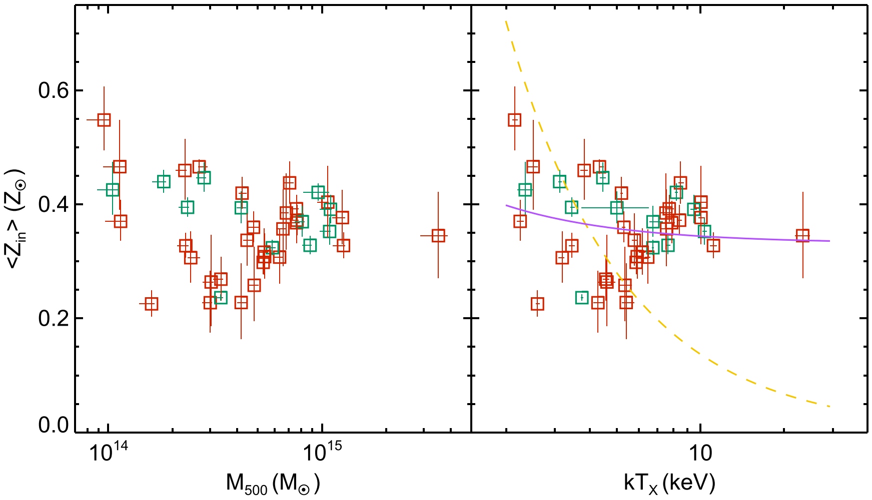

Figure 12. Left: $\bar{Z}_{\mathrm{in}}$ versus M_{500}. Right: $\bar{Z}_{\mathrm{in}}$ versus kT_X. Red points are for NCC clusters, and turquoise points are for CC clusters. The yellow dashed line represents the $\bar{Z}_{\mathrm{in}} - kT_X$ best fit based on the stellar-to-gas mass ratio. The purple line is a similar fit based on stellar-to-gas mass ratio and assuming in addition a baseline pre-enrichment level.

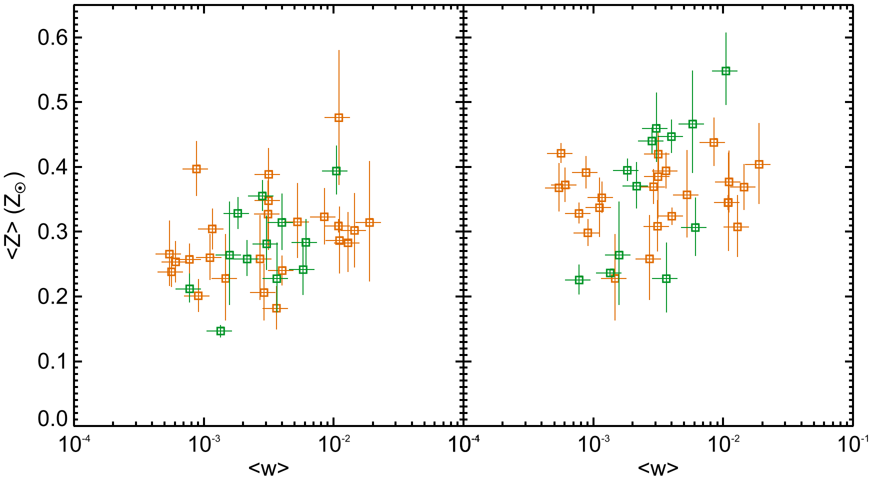

Figure 13. *Left:* $\bar{Z}_{\mathrm{mid}}$ versus $\langle w \rangle$. *Right:* $\bar{Z}_{\mathrm{in}}$ versus $\langle w \rangle$. Green data points in either panel are for low-mass clusters, where $M_{500} < 3.5 \times 10^{14}\, M_{\odot}$. Orange data points are for $M_{500} > 3.5 \times 10^{14}\, M_{\odot}$ clusters.

ICM. A correlation is expected if the population of stars producing the metals detected in X-ray is the same as the one producing the optical luminosity of galaxies.

Dai et al. (2010) fit the temperature–stellar-mass trend to a power law and obtain the following best-fit relation:

$$\log\,(r_{\mathrm{sg}}) = -0.65 - 1.03 \log\left(\frac{kT_X}{1\ \mathrm{keV}}\right). \tag{14}$$

Now, we recall that $\bar{Z}_{\mathrm{in}} = M_{\mathrm{Fe}}^{\mathrm{in}} \big/ (A_{\mathrm{Fe}} M_{\mathrm{gas}}^{\mathrm{in}})$, where $M_{\mathrm{Fe}}^{\mathrm{in}}$ and $M_{\mathrm{gas}}^{\mathrm{in}}$ are the iron and gas masses interior to $r = 0.15 R_{500}$, respectively, and A_{Fe} is the solar iron abundance. We can then write

$$\bar{Z}_{\mathrm{in}} = \frac{M_{*} \langle M_{\mathrm{Fe}}/M_{*} \rangle}{M_{\mathrm{gas}}^{\mathrm{in}} A_{\mathrm{Fe}}}, \tag{15}$$

where M_* is the stellar mass of the cluster, and $\langle M_{\mathrm{Fe}}/M_* \rangle$ is the average iron mass in the ICM per stellar mass. Or, defining $Z_{\mathrm{eff}} = \langle M_{\mathrm{Fe}}/M_* \rangle / A_{\mathrm{Fe}}$, this becomes

$$\bar{Z}_{\mathrm{in}} = Z_{\mathrm{eff}}\, r_{\mathrm{sg}}\big(kT_X\big), \tag{16}$$

where Z_{eff} is the average iron mass in the ICM per stellar mass, scaled by the solar iron abundance, A_{Fe}. The assumption here is that Z_{eff} will be the same for all clusters and will not depend on kT_X.

If we assume that all of the iron inside $0.15 R_{500}$ has been produced by the stars in the galaxies whose luminosities were used by Dai et al. (2010) to measure r_{sg} above, or that at least a population of stars of mass proportional to M_* produced all of the iron observed, then Equation (16) should describe the $\bar{Z}_{\mathrm{in}} - kT_X$ data once scaled by a suitable Z_{eff}.

We perform a least-squares fit of Equation (16) to the data. The purpose of this fit is not to estimate Z_{eff} but simply to test whether the above picture is consistent with our data. We assume equal errors on metallicity measurements so that the results are not largely biased by the data points with smaller uncertainties. The best-fit model, plotted in Figure 12 as the

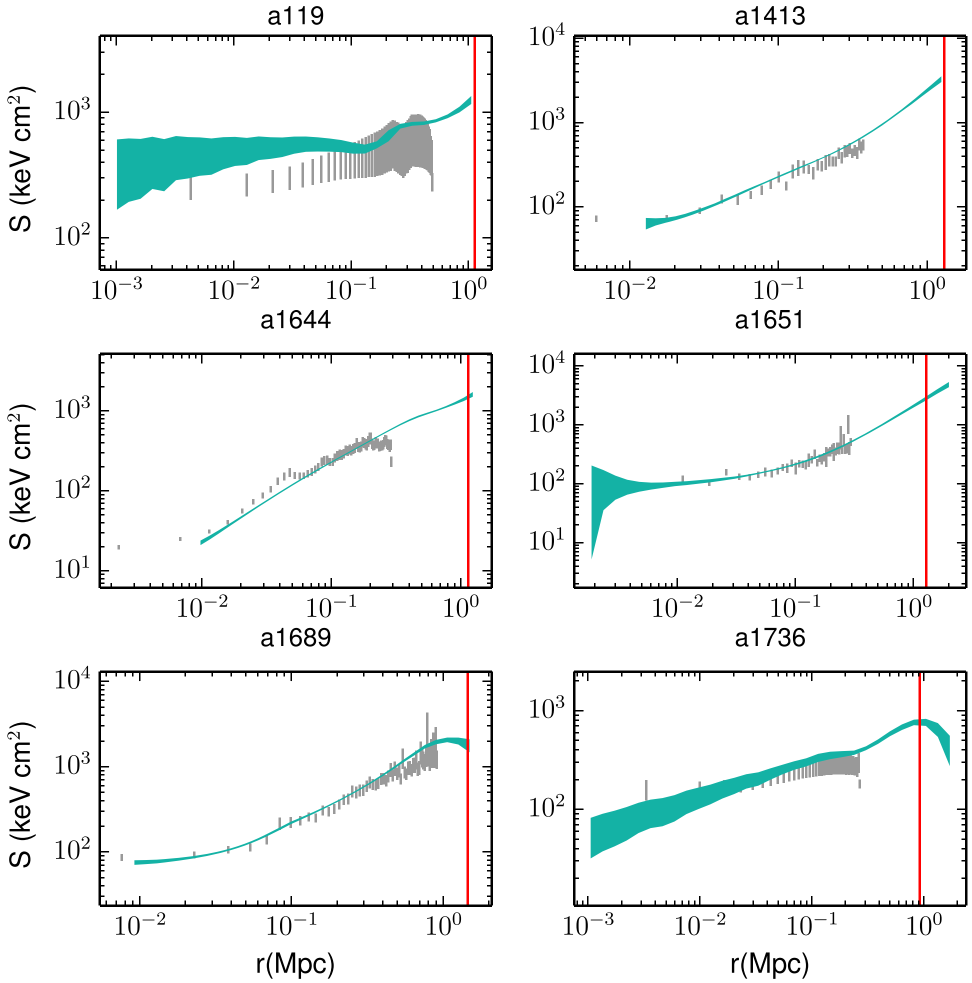

Figure 14. Entropy profiles of the individual clusters in the sample. The turquoise area represents the 68% confidence region computed at various radii, from the temperature and density profiles produced by the Monte Carlo simulations described in Section 2.3.3. The gray error bars are the entropy profile measurements of the ACCEPT study (Cavagnolo et al. 2009). See text for details. The vertical red line is drawn at $r = R_{500}$.

(An extended version of this figure is available.)

dashed yellow line, shows that Equation (16) is an inadequate fit to the observations. Similar to the conclusion in Bregman et al. (2010), this suggests that the stellar population producing the metals within $r = 0.15R_{500}$ is unlikely to be related to the currently observed galaxy population in clusters.

At the risk of having a model too flexible for our data set, we thus introduce another parameter into Equation (16), which is the mean metallicity in the ICM believed to have been set before the current galaxy population started adding more metals. We denote this initial metallicity by $Z_{\rm pre}$. Our model then becomes

$$\bar{Z}_{\rm in} = Z_{\rm eff}\, r_{\rm sg}\left(kT_X\right) + Z_{\rm pre} \tag{17}$$

Unlike Equation (16), Equation (17) fits the high-mass data better *and* passes near the middle of the wide distribution of metallicities of low-mass clusters. The best fit is shown in Figure 12 as the purple line. This gives support to a mass-independent initial metallicity level in the cores of clusters. In this picture, larger clusters would have most of their core metals set by pre-enrichment, as $Z_{\rm pre} \gg Z_{\rm eff}\, r_{\rm sg}$ for large kT_X. Conversely, smaller clusters would have a larger contribution from metals associated with stars, as $Z_{\rm eff}\, r_{\rm sg}\left(kT_X\right)$ increases at low kT_X. The best-fit model has a pre-enrichment value of $Z_{\rm pre} \approx 0.3 Z_\odot$ and a $Z_{\rm eff} \approx 2.\, Z_\odot$. While the value of $Z_{\rm pre}$ agrees with expectations, the large $Z_{\rm eff}$ value again points to the lack of observed galaxies, compared to the observed metals in clusters. The two fits above give similar results when repeated after excluding the bias-suspected clusters, i.e., clusters with $f_{\rm out} < 0.25$.

4.4. Inner Metallicity Boost during Mergers

Finally, we test whether the dispersion in $\bar{Z}_{\rm in}$ is related to dynamic activity, as measured by the centroid shift, $\langle w \rangle$, which is the size of the scatter of the X-ray centroid measured within various apertures around the X-ray peak (e.g., Mohr et al. 1993; O'Hara et al. 2006; Poole et al. 2006), and which is ideal for capturing merger activity (Poole et al. 2006). We find weak evidence for a $\bar{Z}_{\rm in} - \langle w \rangle$ correlation, as we describe below.

Following the prescription in Poole et al. (2006), we calculate the position of the centroid of the X-ray emission within a radius of $0.3R_{500}$, excluding the central 30 kpc. We then calculate the centroid for apertures that are successively smaller by 5% of $0.3R_{500}$. For each aperture, i, we record the distance between the calculated centroid and the X-ray peak, d_i. The centroid shift, $\langle w \rangle$, is then simply the standard deviation of the distances, d_i, scaled by R_{500}. We compute $\langle w \rangle$ for clusters with an FOV that covers $0.3R_{500}$ entirely. We find this radius to

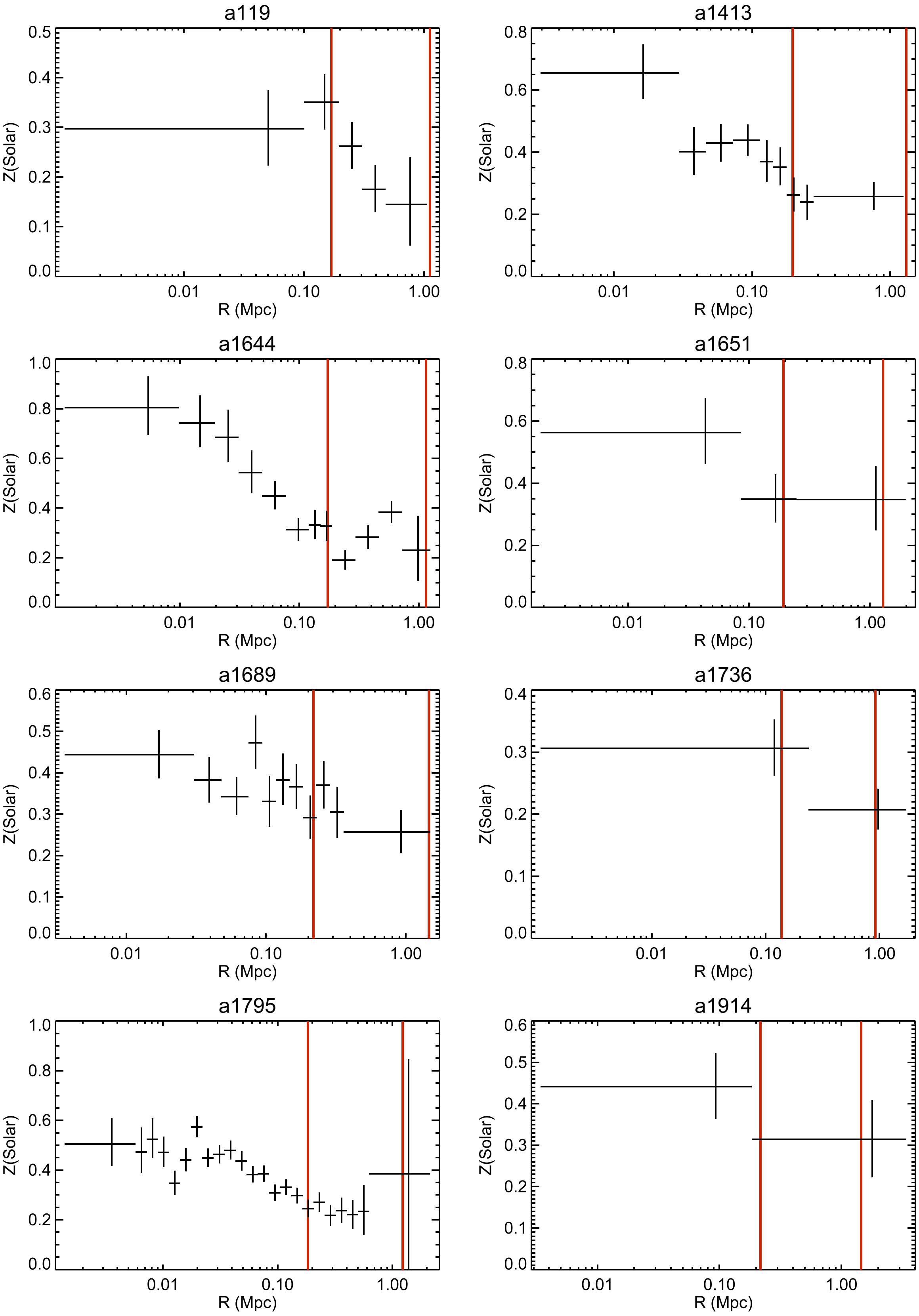

Figure 15. Metallicity profiles of observed *Chandra* clusters. The two vertical red lines are drawn at $r = 0.15R_{500}$ and $r = R_{500}$. See Section 2.3.4 for the details of the metallicity measurement method.

(An extended version of this figure is available.)

Table 6
Cluster Masses and Scales

Cluster	kT_X(keV)	R_{500}(Mpc)	$M_{500}\,(10^{14}\,M_\odot)$	$M_{\mathrm{gas}}\,(10^{13}\,M_\odot)$
Abell 119	$5.79^{+0.1}_{-0.1}$	$1.13^{+0.02}_{-0.02}$	$4.46^{+0.2}_{-0.2}$	$4.50^{+0.1}_{-0.1}$
Abell 1413	$8.42^{+0.1}_{-0.2}$	$1.31^{+0.007}_{-0.03}$	$7.64^{+0.1}_{-0.6}$	$8.11^{+0.1}_{-0.2}$
Abell 1644	$5.31^{+0.05}_{-0.09}$	$1.15^{+0.02}_{-0.02}$	$4.78^{+0.3}_{-0.3}$	$5.50^{+0.2}_{-0.3}$
Abell 1651	$7.52^{+0.4}_{-0.3}$	$1.28^{+0.01}_{-0.03}$	$6.81^{+0.2}_{-0.5}$	$7.30^{+0.2}_{-0.2}$
Abell 1689	$10.4^{+0.2}_{-0.2}$	$1.45^{+0.005}_{-0.05}$	$10.9^{+0.1}_{-1.}$	$12.4^{+0.1}_{-0.4}$
Abell 1736	$3.19^{+0.05}_{-0.09}$	$0.920^{+0.03}_{-0.009}$	$2.43^{+0.3}_{-0.07}$	$2.80^{+0.2}_{-0.1}$
Abell 1795	$6.75^{+0.05}_{-0.05}$	$1.23^{+0.01}_{-0.02}$	$5.86^{+0.2}_{-0.3}$	$6.19^{+0.1}_{-0.1}$
Abell 1914	$10.1^{+0.5}_{-0.5}$	$1.45^{+0.004}_{-0.05}$	$10.7^{+0.1}_{-1.}$	$12.3^{+0.2}_{-0.5}$
Abell 2029	$8.20^{+0.09}_{-0.09}$	$1.44^{+0.06}_{-0.08}$	$9.60^{+1.}_{-1.}$	$12.5^{+2.}_{-3.}$
Abell 2063	$3.45^{+0.08}_{-0.09}$	$0.906^{+0.03}_{-0.009}$	$2.31^{+0.07}_{-0.2}$	$2.36^{+0.07}_{-0.06}$
Abell 2065	$6.18^{+0.2}_{-0.2}$	$1.19^{+0.02}_{-0.02}$	$5.36^{+0.2}_{-0.3}$	$5.80^{+0.1}_{-0.1}$
Abell 2142	$11.2^{+0.3}_{-0.3}$	$1.57^{+0.01}_{-0.06}$	$12.6^{+0.2}_{-1.}$	$14.5^{+0.1}_{-0.6}$
Abell 2147	$4.56^{+0.1}_{-0.1}$	$1.03^{+0.03}_{-0.009}$	$3.37^{+0.07}_{-0.3}$	$3.44^{+0.1}_{-0.08}$
Abell 2163	$23.4^{+1.}_{-1.}$	$2.14^{+0.07}_{-0.1}$	$35.1^{+4.}_{-6.}$	$43.2^{+2.}_{-4.}$
Abell 2204	$9.47^{+0.3}_{-0.3}$	$1.47^{+0.005}_{-0.06}$	$11.0^{+0.1}_{-1.}$	$13.6^{+0.2}_{-0.6}$
Abell 2244	$5.88^{+0.1}_{-0.1}$	$1.18^{+0.02}_{-0.02}$	$5.31^{+0.2}_{-0.3}$	$6.04^{+0.2}_{-0.2}$
Abell 2256	$7.73^{+0.3}_{-0.3}$	$1.37^{+0.03}_{-0.03}$	$8.11^{+0.5}_{-0.6}$	$9.54^{+0.8}_{-0.9}$
Abell 2319	$10.1^{+0.3}_{-0.2}$	$1.58^{+0.01}_{-0.06}$	$12.5^{+0.3}_{-1.}$	$15.6^{+0.3}_{-0.7}$
Abell 2657	$3.82^{+0.1}_{-0.1}$	$0.902^{+0.004}_{-0.03}$	$2.28^{+0.04}_{-0.2}$	$2.08^{+0.05}_{-0.07}$
Abell 2734	$4.28^{+0.2}_{-0.2}$	$0.982^{+0.03}_{-0.007}$	$3.00^{+0.05}_{-0.3}$	$3.02^{+0.1}_{-0.08}$
Abell 3112	$5.01^{+2.}_{-1.}$	$1.09^{+0.02}_{-0.02}$	$4.19^{+0.2}_{-0.2}$	$4.81^{+0.1}_{-0.1}$
Abell 3158	$5.20^{+0.06}_{-0.05}$	$1.10^{+0.02}_{-0.01}$	$4.23^{+0.2}_{-0.1}$	$4.53^{+0.08}_{-0.05}$
Abell 3376	$4.58^{+0.1}_{-0.1}$	$0.964^{+0.03}_{-0.002}$	$2.80^{+0.03}_{-0.2}$	$2.49^{+0.08}_{-0.02}$
Abell 3391	$5.41^{+0.4}_{-0.2}$	$1.10^{+0.02}_{-0.02}$	$4.19^{+0.3}_{-0.2}$	$4.28^{+0.1}_{-0.1}$
Abell 3571	$7.73^{+0.3}_{-0.3}$	$1.35^{+0.01}_{-0.03}$	$7.60^{+0.2}_{-0.5}$	$8.43^{+0.2}_{-0.2}$
Abell 3667	$6.60^{+0.01}_{-0.08}$	$1.32^{+0.01}_{-0.03}$	$7.33^{+0.2}_{-0.5}$	$9.38^{+0.4}_{-0.3}$
Abell 3822	$5.36^{+0.3}_{-0.2}$	$1.15^{+0.02}_{-0.02}$	$4.82^{+0.2}_{-0.3}$	$5.57^{+0.2}_{-0.2}$
Abell 3827	$7.89^{+0.2}_{-0.2}$	$1.33^{+0.01}_{-0.04}$	$7.60^{+0.3}_{-0.6}$	$8.46^{+0.3}_{-0.4}$
Abell 3921	$5.93^{+0.2}_{-0.2}$	$1.18^{+0.02}_{-0.02}$	$5.39^{+0.2}_{-0.3}$	$6.15^{+0.2}_{-0.1}$
Abell 399	$6.47^{+0.1}_{-0.1}$	$1.26^{+0.01}_{-0.03}$	$6.33^{+0.2}_{-0.4}$	$7.43^{+0.1}_{-0.2}$
Abell 400	$2.15^{+0.05}_{-0.04}$	$0.678^{+0.02}_{-0.04}$	$0.955^{+0.07}_{-0.2}$	$0.799^{+0.03}_{-0.07}$
Abell 4038	$3.12^{+0.05}_{-0.03}$	$0.839^{+0.008}_{-0.03}$	$1.82^{+0.05}_{-0.2}$	$1.71^{+0.04}_{-0.09}$
Abell 4059	$4.34^{+0.1}_{-0.02}$	$0.948^{+0.03}_{-0.004}$	$2.66^{+0.2}_{-0.03}$	$2.41^{+0.05}_{-0.07}$
Abell 478	$7.65^{+0.2}_{-0.2}$	$1.39^{+0.006}_{-0.04}$	$8.80^{+0.1}_{-0.7}$	$11.3^{+0.4}_{-0.2}$
Abell 539	$2.59^{+0.04}_{-0.04}$	$0.803^{+0.01}_{-0.03}$	$1.59^{+0.05}_{-0.2}$	$1.63^{+0.1}_{-0.03}$
Abell 644	$8.49^{+0.2}_{-0.1}$	$1.30^{+0.02}_{-0.03}$	$7.06^{+0.3}_{-0.5}$	$6.86^{+0.3}_{-0.3}$
Abell 754	$11.8^{+0.7}_{-0.2}$	$1.33^{+0.05}_{-0.04}$	$7.44^{+0.8}_{-0.8}$	$5.38^{+1.}_{-0.8}$
Abell S 405	$4.62^{+0.3}_{-0.3}$	$0.985^{+0.03}_{-0.007}$	$3.03^{+0.07}_{-0.3}$	$2.85^{+0.09}_{-0.1}$
Hydra A	$3.75^{+0.04}_{-0.03}$	$1.02^{+0.03}_{-0.008}$	$3.36^{+0.08}_{-0.2}$	$4.20^{+0.07}_{-0.1}$
Zw III 54	$2.25^{+0.06}_{-0.06}$	$0.718^{+0.01}_{-0.04}$	$1.14^{+0.07}_{-0.2}$	$1.05^{+0.03}_{-0.09}$
MKW 3 s	$3.44^{+0.09}_{-0.03}$	$0.909^{+0.004}_{-0.03}$	$2.35^{+0.03}_{-0.2}$	$2.43^{+0.03}_{-0.1}$
MKW 8	$2.50^{+0.1}_{-0.1}$	$0.716^{+0.02}_{-0.04}$	$1.13^{+0.07}_{-0.2}$	$0.924^{+0.05}_{-0.07}$
PKS 0745–191	$6.76^{+0.5}_{-0.2}$	$1.35^{+0.01}_{-0.04}$	$8.09^{+0.2}_{-0.6}$	$11.1^{+0.4}_{-0.4}$
UGC 3957	$2.34^{+0.2}_{-0.1}$	$0.697^{+0.02}_{-0.04}$	$1.05^{+0.07}_{-0.2}$	$0.864^{+0.05}_{-0.05}$
ZwCl 1215 + 0400	$7.57^{+0.3}_{-0.3}$	$1.27^{+0.01}_{-0.03}$	$6.57^{+0.2}_{-0.5}$	$6.78^{+0.2}_{-0.2}$
ZwCl 1742 + 3306	$4.46^{+0.1}_{-0.1}$	$0.957^{+0.03}_{-0.006}$	$2.81^{+0.06}_{-0.2}$	$2.61^{+0.07}_{-0.08}$

(This table is available in machine-readable form.)

be a good compromise to include a large area and a good number of clusters. We show the computed $\langle w\rangle$ values in Table 9. Figure 13 shows a plot of $\bar{Z}_{\mathrm{in}}$ versus $\langle w\rangle$ in the right panel. We also include the same plot for $\bar{Z}_{\mathrm{mid}}$ in the left panel of the figure. Data points corresponding to low-mass clusters are in green to distinguish them from the high-mass cluster data points in orange.

Figure 13 suggests that there might be a correlation between $\bar{Z}_{\mathrm{in}}$ and $\langle w\rangle$ for low-mass clusters. Pearson's product-moment correlation coefficient is found to be $r_P = 0.66$, with a p-value of 1.0% for the $\bar{Z}_{\mathrm{in}} - \langle w\rangle$ correlation in clusters with $M_{500} < 3.5 \times 10^{14}\,M_\odot$.

This result suggests an alternative explanation to the $\bar{Z}_{\mathrm{in}}$ dispersion in low-mass clusters, whereby mergers boost measured metallicity. This can be achieved in one of two ways. First, if mergers induce central AGN activity, then we might be observing metals distributed into the central cluster region by the central active engine, as was observed and described in, e.g., Simionescu et al. (2008a, 2009), Kirkpatrick et al. (2009, 2011), and O'Sullivan et al. (2011). This can also be the reason that we observe correlations between $\bar{Z}_{\mathrm{in}}$ and the scaled entropy, x_s, as was shown in Section 3.3. Second, this enhanced central metallicity might simply be the measurement of the central metallicity peak of an infalling subcluster that is not completely merged with the main cluster and whose emission is superimposed on the $r < 0.15R_{500}$ region of the main cluster. In both cases, these effects would need to have a stronger influence on metallicity in low-mass clusters compared to larger clusters.

4.5. Searching for a Pre-enrichment–Preheating Link

The motivation behind undertaking the study of metallicity and entropy as far as possible from the central region—where the influence of the central engine and the effects of cooling increase—was to search for the signature of SNe, which have been heating and chemically enriching the gas surrounding them even before the formation of the galaxy clusters.

The plots of $\bar{Z}_{\mathrm{mid}}$ versus x_s in Section 3.3 show no hint of a relation between the two quantities. However, we note that, for a given radius, the range of values for $x_s = S/S_{\mathrm{grav}}$ can span a range as large as a factor of three at large radii. One can thus envision further study at such large radii to be applied to a larger sample of clusters, which is available in the current *Chandra* archival data. A stacking technique can be used to look for trends between metallicity and excess entropy and to lower any systematics due to the high X-ray background count fraction at such high radii. For example, we could group clusters in bins of S/S_{grav}, where S is measured at a large scaled radius, then extract spectra from each group of clusters from uniform R_{500}-scaled radial bins. These spectra could then be simultaneously fit, assuming they all have the same metallicity at a given scaled radial bin and allowing for the temperatures to vary to match each cluster's temperature. Such a study could be more sensitive to a potential weak trend between metallicity and excess entropy, pointing to the effects of early SN enrichment and heat injection.

5. CONCLUSION

In this work, we analyze a sample of 46 galaxy clusters, extracting chemical and dynamical measurements, in the hopes of obtaining clues about the history of clusters. We measure entropy profiles out to the largest radii where temperature can be measured and provide the best-fit temperature and density profiles for the community to use. We also measure metallicity

Table 7
Best-fit Parameters of the Electron Density Radial Profiles

Cluster	n_0(cm^{-3})	α	β	r_c (Mpc)	r_s (Mpc)	ϵ
Abell 119	0.0005406	0.627	5.0	2.959	0.289	1.227
Abell 1413	0.04096	0.0	0.3753	0.0217	0.3968	2.13
Abell 1644	0.04399	0.9245	0.3237	0.004989	2.17	5.0
Abell 1651	0.009126	0.6828	0.3982	0.08472	0.2506	1.249
Abell 1689	0.04991	0.0	0.399	0.0306	0.3455	1.99

Note. The $n_e(r)$ model is shown in Equation (1).

(This table is available in its entirety in machine-readable form.)

Table 8
Best-fit Parameters of the Temperature Radial Profiles

Cluster	r_t (Mpc)	a	b	c	$a_{\rm cool}$	$r_{\rm cool}$ (Mpc)	$T_{\rm min}$ (keV)	T_0 (keV)
Abell 119	0.2912	−0.3165	4.758	1.011	12.51	0.08264	19.22	8.419
Abell 1413	0.01754	0.4569	6.889	−0.7317	−0.7636	0.1653	1.329	7.881
Abell 1644	0.4703	−0.2443	7.74	0.5485	3.737	0.02752	4.614	6.027
Abell 1651	0.04094	0.04568	4.947	−0.0793	1.9	0.05	6.693	6.858
Abell 1689	1.046	−0.002614	7.542	3.02	8.231	0.07014	10.04	11.45

Note. The $kT(r)$ model is shown in Equation (5).

(This table is available in its entirety in machine-readable form.)

Table 9
Morphological Parameters and Entropy near the Center

Cluster	$c_{\rm SB}$[a]	S_{40}[b](keV cm^2)	$\langle w \rangle$[c]/10^{-3}
Abell 119	2.17 ± 0.037	$550.^{+69.}_{-65.}$	1.12
Abell 1413	9.91 ± 0.079	$112.^{+4.0}_{-3.7}$	0.607
Abell 1644	6.13 ± 0.057	$95.4^{+2.6}_{-2.1}$	(4.60)
Abell 1651	7.71 ± 0.16	$140.^{+4.2}_{-4.0}$	3.15
Abell 1689	12.3 ± 0.064	$108.^{+2.8}_{-2.4}$	1.16

Note. Values of $\langle w \rangle$ in parentheses correspond to measurements in observations where the FOV does not fully cover the region $r < 0.3R_{500}$, and are excluded from analysis involving $\langle w \rangle$, but shown here.

[a] Surface brightness concentration.

[b] Entropy at $r = 40$ kpc.

[c] Centroid shift.

(This table is available in its entirety in machine-readable form.)

profiles for our cluster sample and present them below. The data is made available on an FTP site.[10]

We observe a difference in the scaled iron mass between the centers of low-mass clusters and the centers of high-mass clusters: the values of the iron content in small clusters are more dispersed than those in large clusters. We suggest two possible interpretations of this observation.

1. The lower dispersion in the larger clusters may be a result of the averaging of metallicities from the larger number of halos that have merged to form them. The fact that this effect can be seen even in the cores of clusters lends support to the idea that the centers of clusters continue being enriched by cold and metal-rich gas, originating from the cluster outskirts, even at low redshift.
2. Alternatively, there are hints that clusters can undergo a boost of metallicity during a merger event, which can contribute to the enhancement of metallicity measured in low-mass clusters.

We also look for a connection between the bulk metal content of clusters and their dynamical state, as measured by the deviation of their entropy profiles from a self-similar profile, expected from gravitational shock heating, during cluster formation. We find no evidence of such a relation in our data. More sophisticated studies using a larger sample would be required for such a measurement to obtain more conclusive results.

T.Y.E. would like to thank Michael McDonald for very fruitful conversations.

APPENDIX A
ENTROPY PROFILES

Figure 14 shows individual plots of entropy, as a function of radius, scaled by R_{500}.

APPENDIX B
METALLICITY PROFILES

Figure 15 shows individual plots of metallicity, as a function of radius, scaled by R_{500}.

APPENDIX C
CLUSTER MASSES AND SCALES

Table 6 shows the measured and computed global cluster parameters: X-ray temperature, R_{500}, M_{500}, and M_{gas}.

---

[10] ftp://space.mit.edu/pub/tamer/ebc2015/

Table 10
Global Metallicity Measures

Cluster	$\bar{Z}_{\rm mid}\,(Z_\odot)$	$\bar{Z}_{\rm in}\,(Z_\odot)$
Abell 119	$0.260^{+0.036}_{-0.035}$	$0.337^{+0.047}_{-0.045}$
Abell 1413	$0.253^{+0.032}_{-0.032}$	$0.372^{+0.027}_{-0.026}$
Abell 1644	$0.226^{+0.029}_{-0.028}$	$0.360^{+0.028}_{-0.026}$
Abell 1651	$0.348^{+0.081}_{-0.076}$	$0.385^{+0.069}_{-0.064}$
Abell 1689	$0.304^{+0.032}_{-0.031}$	$0.352^{+0.025}_{-0.024}$
Abell 1736	$0.283^{+0.036}_{-0.034}$	$0.306^{+0.046}_{-0.044}$
Abell 1795	$0.240^{+0.023}_{-0.023}$	$0.324^{+0.013}_{-0.013}$
Abell 1914	$0.314^{+0.095}_{-0.091}$	$0.404^{+0.064}_{-0.061}$
Abell2029	$0.238^{+0.024}_{-0.023}$	$0.421^{+0.015}_{-0.015}$
Abell 2063	$0.187^{+0.024}_{-0.022}$	$0.327^{+0.022}_{-0.021}$
Abell 2065	$0.221^{+0.043}_{-0.040}$	$0.316^{+0.041}_{-0.039}$
Abell 2142	$0.366^{+0.037}_{-0.036}$	$0.328^{+0.023}_{-0.022}$
Abell 2147	$0.290^{+0.038}_{-0.036}$	$0.269^{+0.039}_{-0.037}$
Abell 2163	$0.476^{+0.10}_{-0.10}$	$0.345^{+0.077}_{-0.075}$
Abell 2204	$0.397^{+0.043}_{-0.042}$	$0.391^{+0.025}_{-0.024}$
Abell 2244	$0.201^{+0.026}_{-0.025}$	$0.298^{+0.021}_{-0.020}$
Abell 2256	$0.289^{+0.086}_{-0.078}$	$0.389^{+0.065}_{-0.061}$
Abell 2319	$0.286^{+0.052}_{-0.050}$	$0.377^{+0.049}_{-0.047}$
Abell 2657	$0.281^{+0.043}_{-0.040}$	$0.460^{+0.055}_{-0.051}$
Abell 2734	$0.227^{+0.056}_{-0.052}$	$0.227^{+0.056}_{-0.052}$
Abell 3112	$0.182^{+0.034}_{-0.032}$	$0.394^{+0.029}_{-0.027}$
Abell 3158	$0.389^{+0.026}_{-0.024}$	$0.420^{+0.029}_{-0.027}$
Abell 3376	$0.312^{+0.042}_{-0.040}$	$0.225^{+0.044}_{-0.042}$
Abell 3391	$0.228^{+0.069}_{-0.064}$	$0.228^{+0.069}_{-0.064}$
Abell 3571	$0.191^{+0.034}_{-0.032}$	$0.392^{+0.024}_{-0.023}$
Abell 3667	$0.309^{+0.010}_{-0.010}$	$0.345^{+0.012}_{-0.011}$
Abell 3822	$0.258^{+0.067}_{-0.063}$	$0.258^{+0.067}_{-0.063}$
Abell 3827	$0.265^{+0.052}_{-0.049}$	$0.368^{+0.038}_{-0.036}$
Abell 3921	$0.327^{+0.051}_{-0.049}$	$0.308^{+0.041}_{-0.039}$
Abell 399	$0.283^{+0.047}_{-0.045}$	$0.307^{+0.049}_{-0.046}$
Abell 400	$0.394^{+0.040}_{-0.036}$	$0.548^{+0.059}_{-0.053}$
Abell 4038	$0.355^{+0.025}_{-0.023}$	$0.440^{+0.020}_{-0.019}$
Abell 4059	$0.250^{+0.017}_{-0.016}$	$0.466^{+0.013}_{-0.012}$
Abell 478	$0.257^{+0.025}_{-0.024}$	$0.328^{+0.016}_{-0.015}$
Abell 539	$0.212^{+0.023}_{-0.021}$	$0.225^{+0.024}_{-0.022}$
Abell 644	$0.323^{+0.044}_{-0.042}$	$0.438^{+0.038}_{-0.036}$
Abell 754	$0.302^{+0.058}_{-0.057}$	$0.369^{+0.036}_{-0.035}$
Abell S 405	$0.264^{+0.083}_{-0.077}$	$0.264^{+0.083}_{-0.077}$
Hydra A	$0.147^{+0.0095}_{-0.0094}$	$0.236^{+0.0055}_{-0.0054}$
Zw III 54	$0.258^{+0.029}_{-0.026}$	$0.370^{+0.037}_{-0.034}$
MKW 3 s	$0.328^{+0.025}_{-0.024}$	$0.395^{+0.017}_{-0.017}$
MKW 8	$0.241^{+0.045}_{-0.039}$	$0.466^{+0.082}_{-0.075}$
PKS 0745–191	$0.206^{+0.045}_{-0.043}$	$0.369^{+0.028}_{-0.026}$
UGC 3957	$0.215^{+0.051}_{-0.044}$	$0.426^{+0.049}_{-0.043}$
ZwCl 1215 + 0400	$0.315^{+0.060}_{-0.056}$	$0.357^{+0.069}_{-0.065}$
ZwCl 1742 + 3306	$0.314^{+0.045}_{-0.042}$	$0.447^{+0.026}_{-0.025}$

(This table is available in machine-readable form.)

APPENDIX D
DENSITY AND TEMPERATURE PROFILES BEST-FIT PARAMETERS

Tables 7 and 8 present the best-fit parameters for density and temperature radial profiles, respectively.

APPENDIX E
MORPHOLOGICAL PARAMETERS

Table 9 lists parameters related to the morphology and dynamical state of the clusters. The parameters shown are c_{SB}, S_{40}, and $\langle w \rangle$. See the text and the table notes for details.

APPENDIX F
GLOBAL METALLICITY MEASURES

Table 10 shows the main global metallicity measurements used in this work, $\bar{Z}_{mid}$ and $\bar{Z}_{in}$, for each cluster.

REFERENCES

Anders, E., & Grevesse, N. 1989, GeCoA, 53, 197
Borgani, S., Finoguenov, A., Kay, S. T., et al. 2005, MNRAS, 361, 233
Borgani, S., Fabjan, D., Tornatore, L., et al. 2008, SSRv, 134, 379
Bregman, J. N., Anderson, M. E., & Dai, X. 2010, ApJ, 716, 63
Cavagnolo, K. W., Donahue, M., Voit, G. M., & Sun, M. 2009, ApJS, 182, 12
Cora, S. A. 2006, MNRAS, 368, 1540
Dai, X., Bregman, J. N., Kochanek, C. S., & Rasia, E. 2010, ApJ, 719, 119
De Grandi, S., & Molendi, S. 2001, ApJ, 551, 153
Dickey, J. M., & Lockman, F. J. 1990, ARA&A, 28, 215
Elkholy, T. Y. 2012, PhD thesis, Massachusetts Institute of Technology (http://dspace.mit.edu/handle/1721.1/79425)
Fakhouri, O., Ma, C.-P., & Boylan-Kolchin, M. 2010, MNRAS, 406, 2267
Fujita, Y., Tawa, N., Hayashida, K., et al. 2008, PASJ, 60, 343
Kalberla, P. M. W., Burton, W. B., Hartmann, D., et al. 2005, A&A, 440, 775
Kirkpatrick, C. C., Gitti, M., Cavagnolo, K. W., et al. 2009, ApJL, 707, L69
Kirkpatrick, C. C., McNamara, B. R., & Cavagnolo, K. W. 2011, ApJL, 731, L23
Kravtsov, A. V., Vikhlinin, A., & Nagai, D. 2006, ApJ, 650, 128
Lloyd-Davies, E. J., Ponman, T. J., & Cannon, D. B. 2000, MNRAS, 315, 689
Loewenstein, M. 2006, ApJ, 648, 230
Matsushita, K., Sakuma, E., Sasaki, T., Sato, K., & Simionescu, A. 2013, ApJ, 764, 147
Mazzotta, P., Rasia, E., Moscardini, L., & Tormen, G. 2004, MNRAS, 354, 10
McNamara, B. R., & Nulsen, P. E. J. 2007, ARA&A, 45, 117
Million, E. T., Werner, N., Simionescu, A., & Allen, S. W. 2011, MNRAS, 418, 2744
Mohr, J. J., Fabriant, D. G., & Geller, M. J. 1993, ApJ, 413, 492
Nagai, D., Kravtsov, A. V., & Vikhlinin, A. 2007, ApJ, 668, 1
Nagashima, M., Lacey, C. G., Baugh, C. M., Frenk, C. S., & Cole, S. 2005, MNRAS, 358, 1247
Nath, B. B., & Majumdar, S. 2011, MNRAS, 416, 279
O'Hara, T. B., Mohr, J. J., Bialek, J. J., & Evrard, A. E. 2006, ApJ, 639, 64
O'Sullivan, E., Giacintucci, S., David, L. P., Vrtilek, J. M., & Raychaudhury, S. 2011, MNRAS, 411, 1833
Pointecouteau, E., Arnaud, M., & Pratt, G. W. 2005, A&A, 435, 1
Ponman, T. J., Cannon, D. B., & Navarro, J. F. 1999, Natur, 397, 135
Ponman, T. J., Sanderson, A. J. R., & Finoguenov, A. 2003, MNRAS, 343, 331
Poole, G. B., Fardal, M. A., Babul, A., et al. 2006, MNRAS, 373, 881
Portinari, L., Moretti, A., Chiosi, C., & Sommer-Larsen, J. 2004, ApJ, 604, 579
Pratt, G. W., Arnaud, M., Piffaretti, R., et al. 2010, A&A, 511, 85
Reiprich, T. H., & Böhringer, H. 2002, ApJ, 567, 716
Renzini, A., Ciotti, L., D'Ercole, A., & Pellegrini, S. 1993, ApJ, 419, 52
Santos, J. S., Rosati, P., Tozzi, P., et al. 2008, A&A, 511, 85
Sanders, J. S., & Fabian, A. C. 2006, MNRAS, 371, 1483
Short, C. J., Thomas, P. A., & Young, O. E. 2013, MNRAS, 428, 1225
Simionescu, A., Werner, N., Böhringer, H., et al. 2008, A&A, 493, 409
Simionescu, A., Werner, N., Finoguenov, A., Böhringer, H., & Brüggen, M. 2009, A&A, 482, 97
Simionescu, A., Werner, N., Forman, W. R., et al. 2010, MNRAS, 405, 91
Smith, R. K., Brickhouse, N. S., Liedahl, D. A., & Raymond, J. C. 2001, ApJL, 556, L91
Tozzi, P., & Norman, C. 2001, ApJ, 546, 63
Vikhlinin, A., Markevitch, M., Murray, S. S., et al. 2005, ApJ, 628, 655
Vikhlinin, A. 2006, ApJ, 640, 710
Vikhlinin, A., Kravtsov, A., Forman, W., et al. 2006, ApJ, 640, 691
Voit, G. M., Balogh, M. L., Bower, R. G., Lacey, C. G., & Bryan, G. L. 2003, ApJ, 593, 272
Voit, G. M., Kay, S. T., & Bryan, G. L. 2005, MNRAS, 364, 909
Werner, N., Durret, F., Ohashi, T., & Schindler, S. 2008, SSRv, 134, 337
Werner, N., Urban, O., Simionescu, A., & Allen, S. W. 2013, Natur, 502, 656